

Radio AGN feedback sustains quiescence only in a minority of massive galaxies

Huiling Liu^{1,2}, Yan Lu^{3,4}, Hui Hong^{1,2,5}, Huiyuan Wang^{1,2}, Houjun Mo⁶, Jing Wang⁷, Wanli Ouyang^{3,4}, Ziwen Zhang^{1,2}, Enci Wang^{1,2}, Hongxin Zhang^{1,2}, Yangyao Chen^{1,2}, Qinxun Li^{1,2,8}, Hao Li^{1,2}, Mengkui Zhou^{1,2}

¹*Department of Astronomy, University of Science and Technology of China, Hefei, Anhui 230026, China*

²*School of Astronomy and Space Science, University of Science and Technology of China, Hefei 230026, China*

³*Center of AI for Science, Shanghai AI Laboratory, Shanghai 200233, China*

⁴*Department of Information Engineering, the Chinese University of Hong Kong, Hong Kong, China*

⁵*Department of Physics & Astronomy, University of California, Riverside, CA, 92521, USA*

⁶*Department of Astronomy, University of Massachusetts, Amherst MA 01003-9305, USA*

⁷*Kavli Institute for Astronomy and Astrophysics, Peking University, Beijing 100871, China*

⁸*Department of Physics and Astronomy, The University of Utah, 115 South 1400 East, Salt Lake City, UT 84112, USA*

Radio active galactic nuclei (AGNs) eject a huge amount of energy into the surrounding medium and are thought to potentially prevent gas cooling and maintain the quiescence of massive galaxies¹⁻³. The short-lived, sporadic, and anisotropic nature of radio activities⁴⁻⁷, coupled with the detection of abundant cold gas around some massive quiescent galaxies^{8,9}, raise questions about the efficiency of radio feedback in massive galaxies. Here we present an innovative method rooted in artificial intelligence to separate galaxies in which radio feedback is effective (RFE), regardless of current radio emission, from those in which radio feedback is ineffective (RFI), according to their optical images. Galaxies categorized as RFE are all dynamically hot, whereas quiescent RFI (RFI-Q) galaxies usually have extended cold-disk components. At given stellar mass, dark matter halos hosting RFE galaxies are between four to ten times more massive than those of RFI-Q galaxies. We find, for the first time, that al-

most all RFE galaxies have scant cold gas, irrespective of AGN activity. In contrast, many RFI-Q galaxies are surrounded by substantial amounts of condensed atomic gas, indicating a different evolutionary path from RFE galaxies. Our finding provides direct and compelling evidence that a radio AGN has gone through about 300 on-off cycles and that radio feedback can prevent gas cooling over a timescale much longer than that of radio activity. Contrary to general belief, our analysis shows that only a small fraction of massive galaxies are influenced by strong radio AGNs, suggesting that current galaxy formation models need serious revision.

Feedback from radio AGNs is believed to be capable of inhibiting the cooling and condensation of gas needed for star formation^{7,10,11} and maintaining the quiescence of massive galaxies. The AGN-star formation (AGN-SF) diagram (Figure 1) illustrates this scenario, showing that nearly all galaxies with prominent radio AGN activity (in the upper-left section) are quiescent. Nevertheless, only a small fraction of quiescent galaxies show strong radio emissions¹². Most quiescent galaxies, which are either very faint or undetected in radio, are clustered in the lower-left section of the diagram. Numerous studies attribute this to the radio AGN duty cycle^{2,13,14}, in which even quiescent galaxies lacking radio AGNs today have previously been influenced by radio feedback from past AGN events. However, the potential for radio AGN feedback to prevent gas cooling is derived primarily from energy budget evaluations^{1,3,4}, but direct observational evidence for such feedback is still lacking. If maintenance-mode feedback is indeed efficient in quiescent galaxies, one should expect a deficit of cold gas in these galaxies irrespective of their current AGN activity. This seems in conflict with the fact that some massive early-type/red galaxies do have abundant HI gas^{8,9,15}. From a theoretical perspective, a persistent concern revolves around the ability of sporadic and anisotropic radio jets to adequately inhibit gas cooling^{4,7}, a process that occurs continuously and ubiquitously. This raises the question whether radio feedback is effective in all massive quiescent galaxies or so in only a fraction of such galaxies. The latter question is rarely addressed in the literature and may indicate a large knowledge gap in our understanding of radio AGN feedback and its role in galaxy evolution.

To address the aforementioned question, the key is to have a classification system to distinguish between galaxies where radio feedback has been effective in maintaining quiescence and

those where radio feedback does not have notably impact. For clarity, we refer to the first category as radio-feedback-effective (RFE) galaxies, and the second category as radio-feedback-ineffective (RFI) galaxies. The RFE galaxies, which are quiescent because of radio feedback, comprise two subgroups: galaxies with ongoing and powerful AGN activity (termed RFE-on galaxies) and those with weak or undetectable AGN activity (RFE-off galaxies). They are found along the vertical branch in the AGN-SF diagram. The RFI galaxies also include two subcategories: RFI star-forming (RFI-SF) galaxies and RFI quiescent (RFI-Q) galaxies, both lying along the horizontal branch. It is possible that an RFI galaxy hosts a radio AGN but the radio feedback is not responsible for maintaining its quiescence. In the literature, galaxies are usually categorized as radio or non-radio galaxies, based on their radio emission^{12,14,16}, and as star-forming or quiescent based on the star formation rate^{17,18}. However, these approaches are not applicable in the context concerned here. Both RFE-off galaxies and RFI-Q galaxies exhibit low-level radio activity and star formation, and so occupy the same region in the AGN-SF diagram. Studies based on the synchrotron emission of radio jets and X-ray cavities in the intracluster medium^{5,6,19} found that a single radio-AGN activity lasts for about 10^6 to 10^8 years, a duration significantly shorter than the timescale for stellar evolution and change in galaxy morphology. It is thus anticipated that RFE-off galaxies should have properties similar to RFE-on galaxies. Such similarity is the key we use to separate the two populations, RFE and RFI.

We utilized an artificial intelligence (AI) technique to analyze optical images of quenched low-excitation radio galaxies¹² (hereafter Q-LERGs, see Methods), a representative sample of RFE-on galaxies, and used the training results to identify RFE-off galaxies from the complementary population (non-Q-LERGs) again based on their optical images (Figure 1, see Methods). The galaxy sample and images are taken from the Sloan Digital Sky Survey (SDSS)^{20,21}. We only considered central galaxies, defined as the most massive galaxies of galaxy groups²², to avoid confusion in interpretation. Modern AI, especially deep learning, has been proven capable of classifying objects^{23,24}. However, unlike traditional classification methods, the AI approach learns discriminative feedback-related patterns using only Q-LERG and non-Q-LERG labels, without relying on explicitly labeled RFE or RFI training samples. In our application, the dataset poses a significant challenge due to the combination of imbalanced class distribution, noisy labels, and potential confounding factors. Still, our analysis showed that the model performs well in uncovering

feedback properties of galaxies despite these difficulties, clearly demonstrating the potential of the method for solving similar problems. Based on the model trained with the data augmentation²⁵ and noise-label learning²⁶, we divided the galaxy sample into RFE and RFI populations. The completeness of the RFE galaxies is quite high (85.1%), reflecting the generalization capacity of the model under augmented conditions. We refer to this RFE sample as the complete RFE (cRFE) sample. However, the lower limit of the purity of the cRFE sample is only 29.5%. We thus further selected a high-purity (pRFE) subsample from the cRFE sample by additionally requiring consistent and positive predictions from the non-augmented model. This conservative strategy increases the purity to $> 46\%$, at the cost of reduced completeness (40.3%). The two metrics are better at lower redshift (see Methods).

Figure 2a shows the fraction of RFE galaxies as a function of stellar mass (M_*), using cRFE or pRFE as the sample and taking into account the completeness and purity of the sample (see Methods). Notably, both cRFE and pRFE samples yield similar results. The RFE fraction increases from (0.9 - 7) percent at $\log M_*/M_\odot = 10.6$ to (5 - 30) percent at $\log M_*/M_\odot = 11$. In the most massive bin, nearly all galaxies are RFEs. To examine the role of radio AGNs in maintaining the quiescence of galaxies, we compare the RFE fraction with the fraction of quenched galaxies. In the most massive bin, the RFE and quenched fractions are comparable, suggesting that radio feedback can help maintain quiescence of these galaxies. At $\log M_*/M_\odot \sim 11.5$, the difference between the two fractions becomes visible, while at $\log M_*/M_\odot \sim 11$, the quenched fraction, at about 62 percent, is much higher than the RFE fraction (with a median value of $\sim 17\%$). This clearly indicates that radio feedback cannot explain the quiescence of most galaxies with $\log M_*/M_\odot < 11.5$, and that there must be other channels to keep massive galaxies quiescent. Figure 2c presents the duty cycle fraction, f_{dc} , defined as the ratio in number between the on-duty population (RFE-on) and the total (both on-duty and off-duty) population (RFE-on+RFE-off), for luminous radio AGNs. We are able to obtain this fraction reliably because we have a good control on the RFE-off population. As can be seen, the duty cycle increases from $\sim 1\%$ at $\log M_*/M_\odot = 10.6$ to $\sim 7\%$ at $\log M_*/M_\odot = 11$, and then to $\sim 30\%$ at $\log M_*/M_\odot = 11.8$. These are much larger than the duty-cycle fraction obtained using the traditional method that includes all galaxies of given mass as the total population in estimating f_{dc} . Statistically, f_{dc} is related to the total on-duty (active) duration, t_{on} , and the total off-duty (dormant) duration, t_{off} , as $f_{dc} = t_{on}/t_{RFE}$, where $t_{RFE} = t_{on} + t_{off}$ is the

look-back time since a galaxy became RFE. We thus have $t_{\text{on}} = f_{\text{dc}}t_{\text{RFE}}$ and $t_{\text{off}} = (1 - f_{\text{dc}})t_{\text{RFE}}$. We used the observed f_{dc} to obtain t_{on} and t_{off} assuming $t_{\text{RFE}} = 7.2 \text{ Gyr}$ based on the typical stellar age of RFE galaxies (see Methods), and the results are shown in Figure 2c,d. We compared it with the on-duty duration for single AGN activities²⁷ and found that an RFE galaxy has on average experienced about 300 cycles.

We assessed the difference between RFE and RFI galaxies using results shown in Figure 3. For the RFI population, we focused on RFI-Q galaxies to compare with RFE galaxies that are all quiescent. Since the fraction of RFE-on galaxies in both RFE samples remains consistently low (Figure 2), the results for RFE galaxies are dominated by RFE-offs. The most notable distinction lies in the M_* distribution. RFE galaxies tend to be more massive compared to RFI-Qs. For a fixed M_* , RFE galaxies also possess more massive black holes, have higher concentration and larger axis ratio than RFI-Q galaxies. Our tests revealed that galaxy images in the outskirts are vital for differentiating RFEs from RFIs (see Methods). To confirm this, we analyzed these galaxies using spatially resolved data provided by the MaNGA survey²⁸. The central regions of both RFE and RFI-Q galaxies show similar stellar populations and dynamical properties, as indicated by the 4000Å break (D4000) and velocity dispersion (σ), respectively. In the outskirts, however, the stellar populations of RFE galaxies generally appear older than those of RFI-Q galaxies. The outskirts of RFE galaxies are dynamically hot, similar to their central regions, whereas the outskirts of RFIs are dynamically much colder. The similarity in the axis ratio and kinematics in the outskirts of both RFI-Q and RFI-SF galaxies suggests that the outskirts of RFI-Qs are primarily cold, rotation-supported disks. In contrast, the higher axis ratio and velocity dispersion indicate that RFE galaxies are nearly spherical and dominated by random motion. Our finding aligns with previous studies^{2,29,30}, although they did not differentiate between RFE-off and RFI galaxies.

Earlier research suggests that halos hosting radio galaxies are approximately twice as massive as those hosting other galaxies of the same M_* ³¹. Using weak gravitational lensing³², we obtained the average halo mass (M_{h}) for various populations of galaxies (see Figure 3). At given M_* , the difference in M_{h} between RFE and RFI-Q galaxies is about 0.6 to 1 dex, much higher than previous estimates of about 0.3 dex³¹. This can be attributed to the proficiency of the AI classifier in distinguishing RFE-off from RFI-Q galaxies under the expectation that RFE-offs and RFE-ons

have similar M_h . These results suggest that the global efficiency to convert gas into stars, characterized by M_*/M_h , is about 4 to 10 times higher in RFI galaxies than in RFE galaxies, consistent with that AGN feedback is much more effective in RFE galaxies than in RFIs. It has been proposed recently that the M_h - M_{BH} relation can provide insight into AGN feedback mechanisms^{33,34}. We thus also present such relations based on our data. At fixed M_{BH} , the difference in M_h between the RFE and RFI-Q galaxies ranges from 0.6 to 0.8 dex. More interestingly, the RFE and RFI galaxies appear to reside in distinct halo populations, with a division at $M_h \sim 10^{12.8} M_\odot$. This demonstrates that M_h plays an important role in radio feedback, potentially more than M_* and M_{BH} . One possibility is that the higher merger rate in more massive halos enhances the spin of supermassive black holes, thereby facilitating the launching of radio jets³⁵. Alternatively, the increase in the amount of hot gas in more massive halos may promote AGN formation and feedback.

The galaxy images used in the AI learning are not expected to carry any direct information related to M_h . Therefore, the large difference in M_h between RFEs and RFIs thus testifies to the robustness of our AI classification. At fixed M_* , the halo and galaxy characteristics of both pRFE and RFE-on galaxies are very similar, consistent with our AI method’s verdict that RFE-off and RFE-on galaxies are similar in galaxy and halo properties. The difference between cRFE and RFE-on galaxies is marginally larger, probably due to the elevated contamination in the cRFE sample.

The success of our AI method in separating RFE and RFI galaxies provides a unique opportunity to study the impact of radio feedback on galaxies. Should radio AGN feedback be capable of effectively heating the circumgalactic medium (CGM), there must be large difference in the cold gas component between RFE and RFI galaxies. To test this explicitly, we compared the HI content between these two populations of galaxies. Figure 4 shows the HI gas fraction, M_{HI}/M_* , provided by the xGASS survey³⁶. Given that most RFE galaxies have $\log M_*/M_\odot > 10.5$, our analysis was restricted to galaxies above this mass limit. The HI gas fraction increases progressively as the sample changes across the sequence pRFE, cRFE, RFI-Q, and RFI-SF. Most pRFE galaxies are deficient of HI gas, with $\log M_{\text{HI}}/M_* < -1.7$. Of the 42 pRFE galaxies with available xGASS data, only one has $\log M_{\text{HI}}/M_* > -1.5$ (thus gas-rich). Among the 106 cRFE galaxies, 15 are classified as gas-rich, and the larger gas-rich fraction is probably due to larger contamination in this sample.

Within the subset of 6 RFE-on galaxies, none is gas-rich. In contrast, 38% of RFI-Q galaxies and 90% of RFI-SF galaxies are rich in HI gas. The gas-rich threshold is set to be $\log M_{\text{HI}}/M_{\star} = -1.5$, because the distribution of star-forming galaxies quickly declines around this value (Figure 4d).

To mitigate potential dependence on M_{\star} , we randomly chose one RFI-Q galaxy that matches each pRFE or cRFE galaxy in M_{\star} , and constructed a total of 1000 control samples of RFI-Q galaxies in this way. For each control sample, we computed the fraction of gas-rich galaxies. As shown in Figure 4, the median value of the gas-rich fraction is 36% (37%) for control samples constructed to match pRFE (cRFE). Even the lowest values obtained from the control samples for pRFE and cRFE, 14% and 23% respectively, are much larger than the values for the pRFE and cRFE samples themselves. Several studies have found that the HI gas fraction has the strongest correlation with the NUV-r color³⁶, M_{BH} ³⁷ and the linear combination of NUV-r and stellar mass density³⁸. We constructed control samples from RFI-Q by matching NUV-r color with pRFE or cRFE galaxies. The samples controlled in NUV-r have gas-rich fractions peaked at 20%. None/0.4% of the control samples have a gas-rich fraction lower than that of pRFE/cRFE galaxies. Similar trends are found for samples controlled in M_{BH} or both NUV-r and stellar mass density. Thus, the radio feedback that underpins the AI-based RFE/RFI classification is more important than M_{BH} and the NUV-r color in determining the amount of cold gas.

The analyses so far have ignored potential impact by misidentification. The intrinsic difference between RFE and RFI-Q galaxies should, therefore, be even larger. Assuming that the misidentification is insensitive to the HI content for quiescent galaxies, we evaluated the RFE fraction in gas-poor galaxies ($\log M_{\text{HI}}/M_{\star} < -1.5$). As shown in Figure 2b, the dependence on M_{\star} becomes much weaker in comparison to the total population. The typical value of the RFE fraction at $\log M_{\star}/M_{\odot} > 10.8$ is around 60%, close to unity, although the uncertainty is large. This indicates that the majority of gas-poor galaxies are indeed RFE galaxies and most of RFI-Q galaxies are gas-rich. Since RFE galaxies on average reside in more massive halos than RFI galaxies of the same M_{\star} (Figure 3), without radio heating RFE galaxies would contain larger amount of HI gas because of the higher cooling rate in their more massive halos¹, which is in conflict with the observations presented here. This, of course, is the reason why we believe that heating sources are needed for RFE galaxies to counterbalance cooling. Furthermore, the predominance of RFE-

off galaxies among the RFE population suggests that AGN feedback can effectively prevent gas cooling even after the AGN activity is paused. Therefore, despite of its sporadic and anisotropic nature, radio feedback seems able to compensate the radiative loss that has much larger temporal and spatial scales than the feedback itself. These results give strong support to the hypothesis that feedback from strong radio AGNs can effectively heat the CGM, impeding gas cooling and maintaining the quiescence of host galaxies.

However, radio heating is ineffective in the majority of massive quiescent (RFI-Q) galaxies. Many of these galaxies contain abundant cold gas (Figure 4), either cooled from the CGM or acquired from stripped satellite galaxies³⁹, which is sustainable in the absence of strong radio heating. It is also plausible that the cold gas in some RFI-Q galaxies is the gas that existed prior to quenching. In the former case, the rotational axis of newly acquired gas is expected to have some misalignment with that of the stellar component, whereas in the latter case, the left-over gas should show alignments with the stellar component. The ATLAS^{3D} HI project conducted a HI survey of local early-type galaxies⁸, and found that a significant fraction of these galaxies show misalignment between HI and stellar components^{8,40}. Among the total of seven galaxies that are quenched and gas rich, five or six exhibit rotational misalignment, and one displays irregular HI morphology (see Methods). Thus, the cold gas in massive quiescent galaxies is likely acquired recently, corroborating the hypothesis of absence of strong radio heating.

Because of significant differences in their radio activity, galaxy, halo and HI-gas properties, it is likely that RFI-Q galaxies have different evolutionary paths than RFEs, particularly in connection to the maintenance of quiescence. One possible way for the gas-rich RFI-Q galaxies to maintain quiescence is that the cold gas has large angular momentum, so that the HI disk is too large to form stars and to feed the central black hole^{8,41}. Indeed, all seven gas-rich and quenched galaxies in the ATLAS^{3D} HI project have HI disks much larger than their stellar components (see Methods)⁸. It is also possible that most of the CGM gas of some RFI-Q galaxies has already been consumed by star formation⁴², as indicated by the large M_*/M_h (Figure 3), so that remaining CGM is too diffuse to cool. For example, in the elliptical galaxy NGC 720, only about $10^9 M_\odot$ of the gas can cool over 5 billion years according to the prediction of a model without radio heating¹. Figure 4 shows that many RFI-Q galaxies have HI masses similar to RFI-SF galaxies. This sug-

gests that RFI-Q galaxies may resume their star formation^{43,44}, in contrast to RFEs which remain quenched. The small D4000 in the outskirts of some RFI-Q galaxies (Figure 3) may signify the onset of rejuvenation. These galaxies are currently forming stars in the outskirts dominated by newly accreted, high angular momentum gas in an extended distribution⁸. It is thus likely that a fraction of star-forming galaxies are rejuvenated galaxies. This may explain the large ranges of concentration, outskirt dynamical states, and inner D4000 covered by RFI-SF galaxies in comparison to other types of galaxies (Figure 3).

Many current galaxy formation models assume a radio (kinetic) mode of AGN feedback to heat the CGM and suppress gas cooling in massive galaxies^{10,11,45}. Such feedback is invoked to sustain the quiescence of almost all massive galaxies⁴⁶. These models are thus at odds with our discovery that RFE galaxies constitute only a small fraction of all quenched massive galaxies (Figure 2) and that gas cooling may be effective in RFI-Q galaxies. One possible reason for the failure of these galaxy formation models is that the triggering of radio AGNs and feedback is not correctly modeled. Our results demonstrate that strong radio AGNs can be triggered mainly in entirely dynamically hot, massive galaxies that live in massive halos, in contrast to the assumption of many models that radio-AGN feedback becomes effective as soon as the mass of central super-massive black holes reaches some threshold^{11,47}. Clearly, some of the model assumptions need to be modified, and our results provide impetus for the search of a viable model.

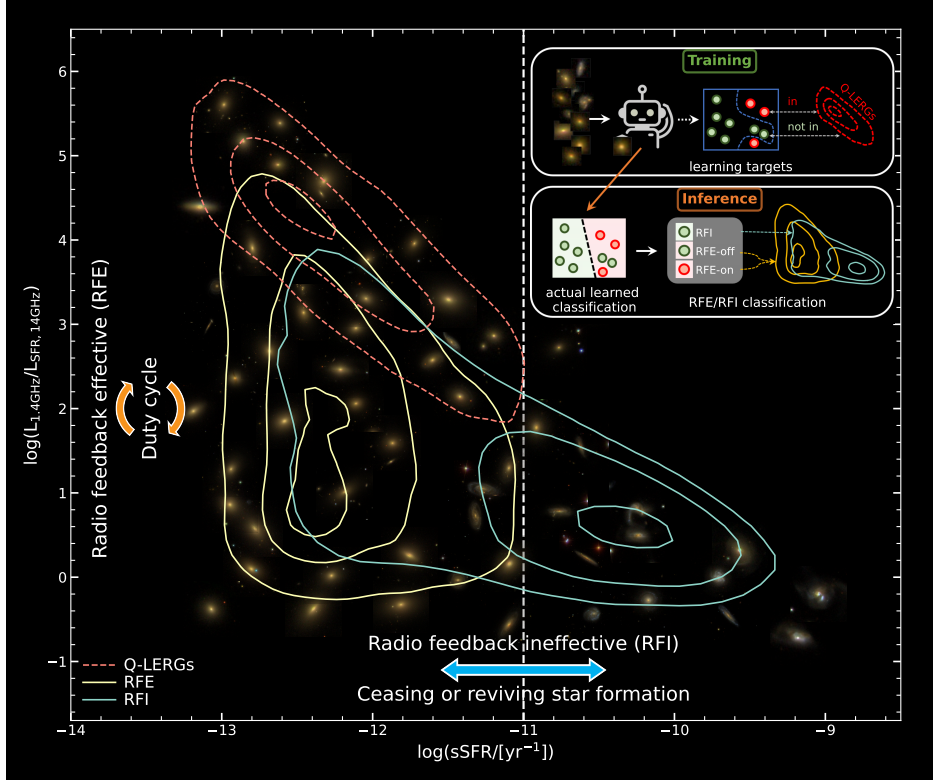


Figure 1: **AGN-SF diagram and AI pipeline.** The observed radio luminosity ($L_{1.4\text{GHz}}$) scaled by the predicted radio luminosity ($L_{\text{SFR},1.4\text{GHz}}$) from the star-formation rate (SFR) ⁴⁸ versus the specific star-formation rate (sSFR). The red dashed contours exhibit Q-LERGs, a representative sample of RFE-on galaxies. The cyan and yellow contours show the RFI and RFE (cRFE) populations, which are the outcome of the AI analysis. The contour lines enclose 10%, 50% and 90% of the galaxies with $\log M_*/M_\odot > 10.5$. See Methods for more details, particularly for how we assign $L_{1.4\text{GHz}}$ to radio-undetected galaxies. The vertical dashed line indicates the demarcation between quiescent and star-forming galaxies. RFE galaxies may move vertically as they enter the duty cycle of AGN activity on a short timescale^{5,6}, while RFI galaxies can move horizontally as their star formation rates evolve (usually with a longer timescale). We show the images of randomly selected galaxies in the background. Most star-forming galaxies are blue and exhibit spiral arms; most galaxies with large $L_{1.4\text{GHz}}/L_{\text{SFR},1.4\text{GHz}}$ are red and appear to be elliptical galaxies; both elliptical and disk-like galaxies exist in the lower-left section of the diagram. The RFE classifier, which is trained by Q-LERG labels only, can classify RFE and RFI based on SDSS galaxy images. This is achieved by combining both training the model to classify Q-LERG (RFE-on) versus non-Q-LERG (RFE-off + RFI) and deliberately encouraging the model to misclassify RFE-offs into the Q-LERG category through a noise-label learning scheme. Since RFE-off and Q-LERG galaxies share similar optical appearance in the image domain, we successfully generated an RFE classifier that distinguishes RFE (RFE-on + RFE-off) from RFI. See Extended Data Table 1 for the introduction of the terminologies and samples used in this paper.

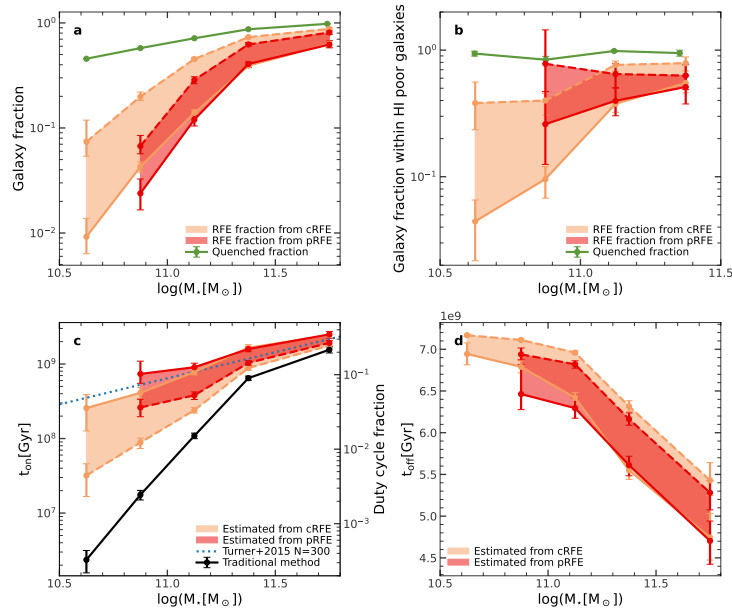


Figure 2: **Galaxy fractions and duty cycle.** Panel a: fractions of quenched galaxies (green), RFE galaxies estimated from the pRFE sample (red) and the cRFE sample (orange) as functions of M_* . Panel b: quenched and RFE fractions in the gas-poor population of galaxies ($\log M_{\text{HI}}/M_* < -1.5$). Panel c: the on-duty duration time (t_{on} , left vertical axis) and duty cycle fraction (right axis) for radio galaxies with $L_{1.4\text{GHz}} > 10^{23} \text{W Hz}^{-1}$. Panel d: the off-duty duration time (t_{off}) as functions of M_* . Error bars represent the 16th–84th percentiles of 150 bootstrap samples. The dashed line (red or orange) is obtained by assuming 100% purity and the solid line corresponds to the lower limit of the purity (see Methods). Results in panels a, c and d are obtained using all galaxies at redshift $z < 0.091$. Under this redshift cut, galaxies are complete for $\log M_*/M_\odot > 10.5$ in optical data and for $L_{1.4\text{GHz}} > 10^{23} \text{W Hz}^{-1}$ in radio data. The results in panel b are based on xGASS galaxies that have $z < 0.05$, and the completeness and purity used here are both estimated using galaxies with $z < 0.05$. The RFE galaxy fraction in the total population depends more strongly on M_* than the quenched fraction. For the cold gas-poor galaxies, the RFE fraction is large, close to unity, and almost independent of M_* at $\log M_*/M_\odot > 10.8$. In panel c, t_{on} for RFE galaxies is derived from duty cycle result, assuming a total RFE timescale of $t_{\text{RFE}} = 7.2 \text{ Gyr}$ (see Methods). The blue dashed lines represent the $t_{\text{on}} - M_*$ relation from the ref.²⁷, originally derived for a single feedback cycle. Here we scale this relation by 300 to match our result. This suggests that, on average, an RFE galaxy has experienced ~ 300 cycles. Moreover, $t_{\text{off}} = t_{\text{RFE}} - t_{\text{on}}$ is much longer than t_{on} .

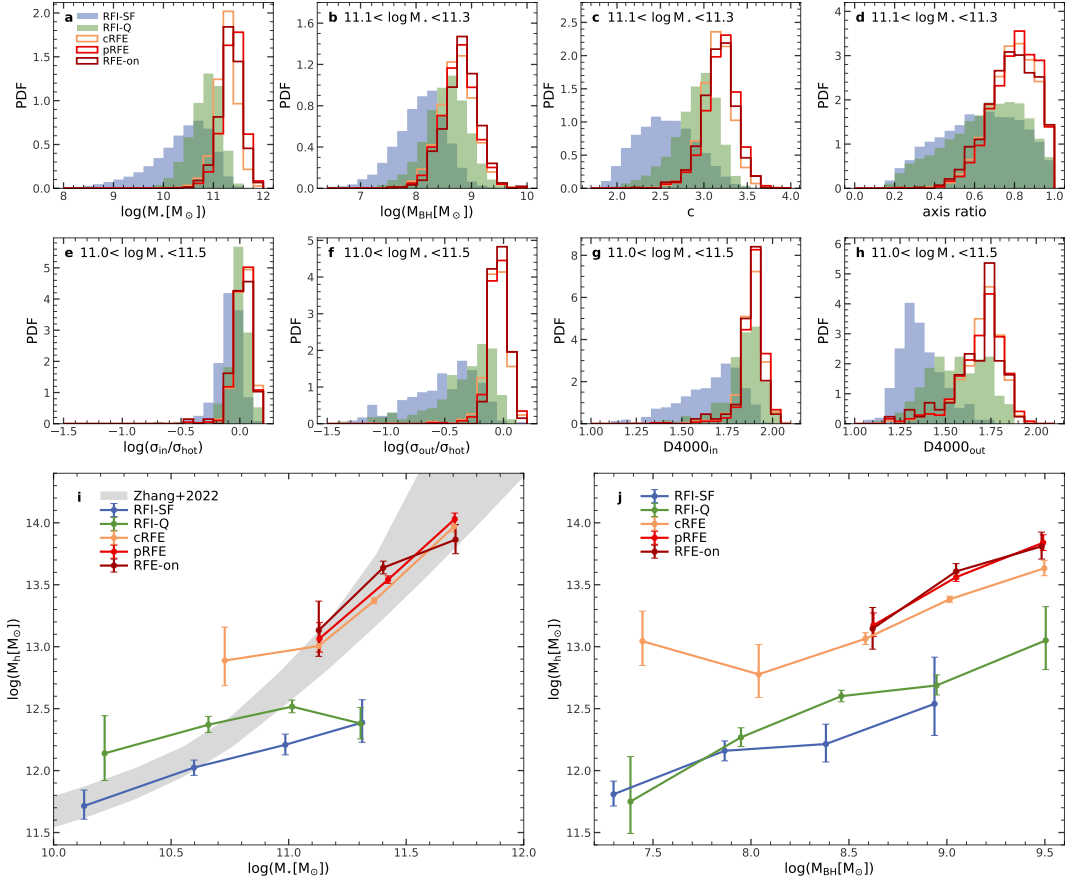


Figure 3: **Galaxy and halo properties of RFE and RFI galaxies.** Panel a: the probability distribution of M_* for RFE-on (wine), pRFE (red), cRFE (orange), RFI-Q (green) and RFI-SF (blue) galaxies. Panels b-d: the distributions of M_{BH} , concentration and axis ratio for the five types of galaxies with $11.1 < \log M_*/M_\odot < 11.3$. Panels e-h: the distributions of spatially-resolved galaxy properties for the five types of galaxies with $11.0 < \log M_*/M_\odot < 11.5$, including the stellar velocity dispersion in the inner (σ_{in}) and outer regions (σ_{out}) scaled with the velocity dispersion (σ_{hot}) of a dynamically hot system at the same M_* ³⁰, and the 4000Å break in the inner and outer regions. A system is dynamically hot if its velocity dispersion is comparable to σ_{hot} , otherwise it is dynamically cold, usually dominated by rotational motion. Note that results in other M_* bins are similar but not plotted. Panels i-j: the M_* - M_{h} and M_{BH} - M_{h} relations, where halo masses are estimated using weak gravitational lensing technique. The shaded region represents the combination of several empirical M_* - M_{h} relations⁴². We only show results for bins with errors less than 0.5 dex and with galaxy numbers above 100. Error bars represent the 16th–84th percentiles of 150 bootstrap samples. In general, RFE galaxies are different from RFI galaxies in dynamics, stellar population, morphology and halo mass. Both pRFE and cRFE galaxies exhibit similar properties to RFE-on galaxies.

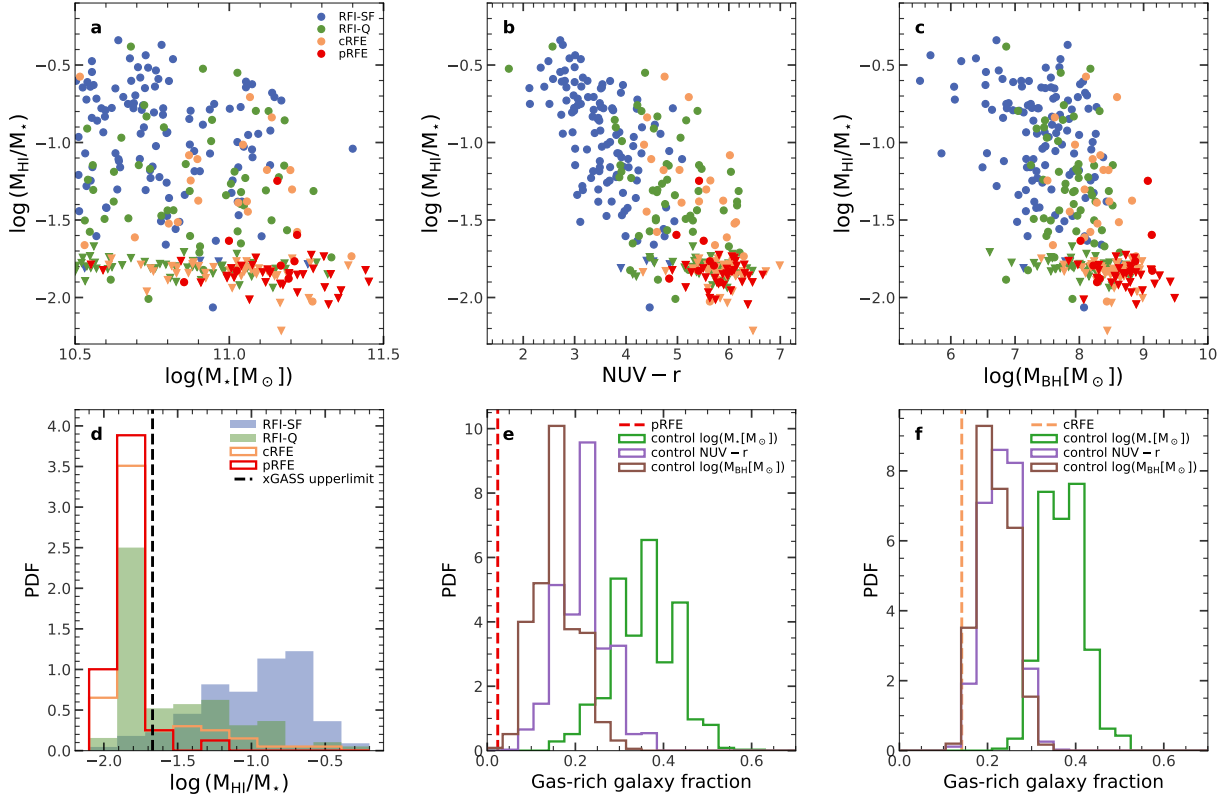


Figure 4: **The HI-gas fraction.** Panels a-c: the HI gas fraction ($\log M_{\text{HI}}/M_*$, obtained from the xGASS survey³⁶) as a function of various galaxy properties: stellar mass M_* , NUV-r color, and black hole mass M_{BH} . Triangle symbols show upper limits of $\log M_{\text{HI}}/M_*$. Panel d: the histograms of $\log M_{\text{HI}}/M_*$ for xGASS galaxies. The dashed black vertical line shows the maximum value of the upper-limits. In panels a-d, red is for pRFE, orange for cRFE, green for RFI-Q and blue for RFI-SF. Panel e: the distribution of the gas-rich fraction (fraction of galaxies with $\log M_{\text{HI}}/M_* > -1.5$ in a sample). The vertical dashed line shows the result for the pRFE sample. The histograms show distributions of control samples selected from the RFI-Q sample to match the pRFE sample in M_* (green), NUV-r (purple) and M_{BH} (brown), respectively. Panel f: similar to panel e but showing results for cRFE galaxies. All the results are based on galaxies with $\log M_*/M_\odot > 10.5$. The AI-selected RFE galaxies have much less HI gas than RFI-Q galaxies at given M_* , M_{BH} or NUV-r color. Since most of the gas-poor galaxies are RFE galaxies after the correction of misidentification (Figure 2), the real gas-rich fraction of RFI-Q galaxies is much larger than that shown here. Note that there are only 6 RFE-on galaxies, we do not show them separately.

Methods

Galaxy samples and galaxy properties Our galaxy sample was taken from the New York University Value Added Galaxy Catalog (NYU-VAGC) sample⁴⁹ of the Sloan Digital Sky Survey (SDSS) DR7²¹. Galaxies with r -band Petrosian magnitudes $r \leq 17.72$, with redshift completeness > 0.7 , and with redshift range of $0.01 \leq z \leq 0.2$, are selected. We only focused on central galaxies, defined as the most massive galaxies within dark matter halos, identified according to the halo-based group-finding algorithm^{22,50}. The NYU-VAGC catalog also provides spectroscopic velocity dispersions σ_* , rest-frame colors $^{0.1}(g - r)$, which are k -corrected to $z = 0.1$, and the measurements of the sizes of each galaxy, R_{50} and R_{90} , which are the radii enclosing 50 and 90 percent of the Petrosian r -band flux of the galaxy, respectively. The central velocity dispersion σ_c within $R_{50}/8$ is estimated from σ_* using $\sigma_c = \sigma_*(R_{50}/8R_{\text{ap}})^{-0.066}$, where $R_{\text{ap}} = 1.5''$ is the size of SDSS spectroscopic fiber⁵¹. The concentration of a galaxy is defined as $c = R_{90}/R_{50}$, usually used to indicate the morphology of the galaxy⁵². The mass of the central supermassive black holes is estimated as⁵³

$$\log M_{\text{BH}}[M_{\odot}] = 5.246 \log \sigma_c[\text{km/s}] - 3.77. \quad (1)$$

We cross-matched our sample with the MPA-JHU DR7 catalog to obtain the measurements of the stellar mass, M_* , which is obtained by fitting the SDSS $ugriz$ photometry⁵⁴. The GSWLC⁵⁵ provides SFR for SDSS galaxies, and we used the SFR from the GSWLC-2 version, obtained by fitting the UV+optical+mid-IR SEDs. We adopted $\log(s\text{SFR}[\text{yr}^{-1}]) = -11$ to separate quiescent/quenched galaxies from star-forming galaxies, where $s\text{SFR} = \text{SFR}/M_*$. The axis ratios, which describe the projected ellipticity of galaxies, are obtained by cross-matching our sample with the `PhotoObjAll` table of SDSS DR12⁵⁶. We downloaded the SDSS optical images for these galaxies from the SDSS website. Each galaxy image is positioned at its center, with a size equal to 6 times R_{50} (512 pixels on each side). These images are constructed from the SDSS data in the g , r and i bands to form 3-color jpg images using the published pipeline⁵⁷. In the following, we use galaxy images for AI training. The image size is chosen as stated above to ensure that both the central and peripheral regions of galaxies are included in the AI learning process, while minimizing the influence of other galaxies or objects. Our final central galaxy sample consists of 400,309 galaxies, among which 259,148 have $M_* \geq 10^{10.5}M_{\odot}$.

We cross-matched our galaxy sample with the local radio source sample¹², which has been widely used to study the properties, distributions, and evolution of radio galaxies². This radio source sample was assembled from the SDSS DR7 and the National Radio Astronomy Observatory’s Very Large Array Sky Survey (NVSS)⁵⁸, as well as the Faint Images of the Radio Sky at Twenty Centimeters (FIRST) survey⁵⁹. A total of 5,506 central galaxies are detected at 1.4GHz. According to the classification in the literature¹², 3,797 central galaxies are classified as radio AGNs. There are two fundamentally different radio AGN classes, ‘Low-Excitation Radio Galaxies’ (LERGs) and ‘High-Excitation Radio Galaxies’ (HERGs). About 3% of radio galaxies are classified as HERGs, and 10% unclassified. HERGs have Eddington ratios between one and ten percent and are usually associated with younger stellar populations, indicating that they are unlikely to be responsible for maintaining the long-term quiescence in their host galaxies. In contrast, LERGs exhibit lower Eddington ratios (mostly below 1%) and tend to reside in more massive galaxies with older stellar population¹². Since our purpose is to investigate the role of the maintenance-mode AGN feedback, which is believed to be capable of maintaining the quiescence of its host galaxy, we consider only quenched LERGs, labeled Q-LERG. Almost all of these galaxies are red, and 6 galaxies with blue color ($^{0.1}(g - r) < 0.7$) are also excluded. There are 3,095 Q-LERGs, and the rest 397,214 galaxies in our sample are labeled non-Q-LERG. About 93% of the Q-LERGs have radio luminosity at 1.4 GHz ($L_{1.4\text{GHz}}$) higher than 10^{23}W Hz^{-1} . Therefore, the Q-LERG sample is dominated by radio galaxies with powerful radio activity. Should radio feedback truly suppresses gas cooling, it must show efficacy in the Q-LERG sample. We thus use the Q-LERG sample as a representative sample for RFE-on galaxies. The terminologies and samples used in this paper are listed in Extended Data Table 1.

The AGN-SFR diagram The AGN-SFR diagram in Figure 1 shows $L_{1.4\text{GHz}}/L_{\text{SFR},1.4\text{GHz}}$ versus the specific star formation rate ($s\text{SFR}$). Here, we describe how we constructed the figure. $L_{\text{SFR},1.4\text{GHz}}$ is the expected 1.4GHz luminosity powered by the star formation⁴⁸:

$$\log(L_{\text{SFR},1.4\text{GHz}}[\text{W/Hz}]) = 1.52 \log(\text{SFR}[\text{M}_{\odot}/\text{yr}]) + 21.24. \quad (2)$$

Extended Data Fig. 1 shows this relation and the distributions of galaxies detected and undetected in radio emission. The radio-detected galaxies exhibit two distinct populations. One is close to the $L_{\text{SFR},1.4\text{GHz}}$ -SFR relation while the other has $L_{1.4\text{GHz}}$ much larger than $L_{\text{SFR},1.4\text{GHz}}$, indicative

Extended Data Table 1: Terminologies and samples used in this paper

Name	Description	Number
Classification using radio activity and star formation		
Q-LERG	quiescent Low-Excitation Radio Galaxies	3,095
non-Q-LERG	galaxies not classified as Q-LERG	397,214
Feedback efficacy classification using AI		
RFE	Radio-feedback-effective galaxies	
RFE-on	Q-LERGs, RFE galaxies with powerful radio activity	3,095
RFE-off	RFE galaxies with undetectable AGN activity	
pRFE-off	High purity RFE-off sample	8,693
cRFE-off	High completeness RFE-off sample	38,784
pRFE	RFE-on and pRFE-off	11,788
cRFE	RFE-on and cRFE-off	41,879
RFI	Radio-feedback-ineffective galaxies	358,430
RFI-Q	Quiescent RFI galaxies	121,442
RFI-SF	Star-forming RFI galaxies	236,988

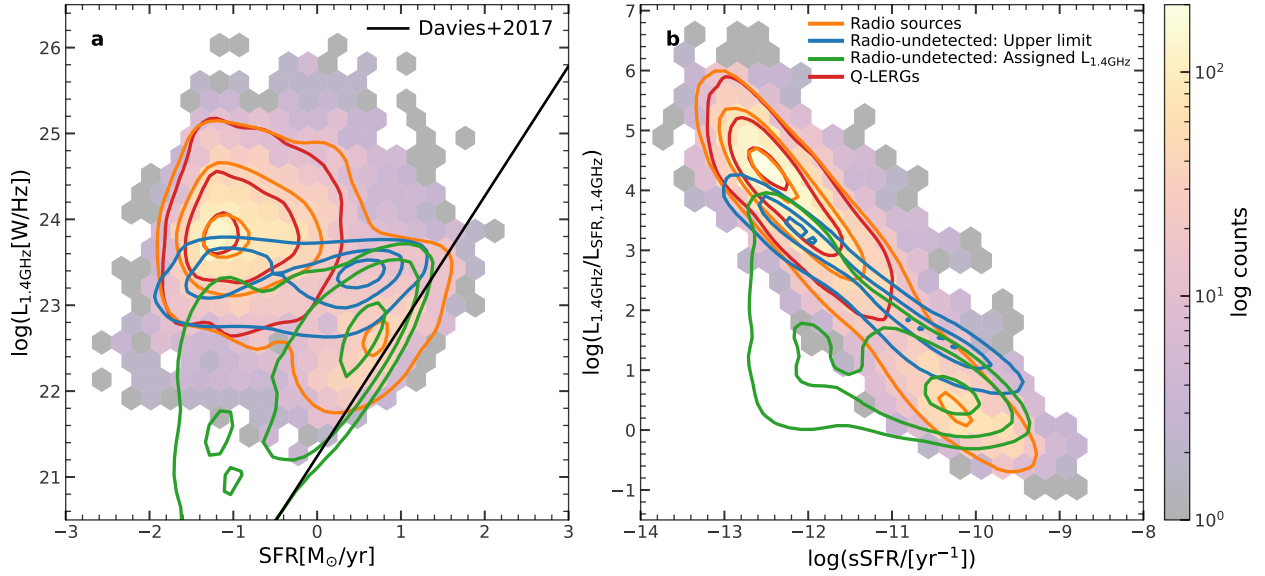
All galaxies are central galaxies of galaxy groups. Q-LERGs and non-Q-LERGs are classified by using the radio activity and SFR. The non-Q-LERG sample comprises cRFE-off and RFI samples. We utilized the AI to classify galaxies into RFE (RFE-on+RFE-off) and RFI(RFI-Q+RFI-SF) samples. The RFE-on sample is exactly the same as the Q-LERG sample. Because of the difficulties discussed in the text, we actually obtained two RFE-off samples, pRFE-off(higher purity) and cRFE-off(higher completeness), and therefore two RFE samples, pRFE and cRFE. Note that the pRFE-off (pRFE) sample is the subset of the cRFE-off (cRFE) sample.

of the contribution of radio AGNs. We also presented the distribution of the upper limit (L_{lim}) of $L_{1.4\text{GHz}}$ for the radio-undetected galaxies. L_{lim} for each galaxy is derived from the flux limit¹² of 5 mJy and the redshift of the galaxy,

$$L_{\text{lim}} = 4\pi D_L^2(z) F_{\text{lim}} (1+z)^{-\alpha-1}, \quad (3)$$

where D_L is the luminosity distance, and $\alpha = -0.7$ is the typical spectral index⁶⁰. We assign a mock $L_{1.4\text{GHz}}$ to radio-undetected galaxies as follows. For each of these galaxies, we first generate a radio luminosity of $L_{\text{SFR,pred}}$ based on its SFR using the $L_{\text{SFR,1.4GHz}} - \text{SFR}$ relation⁴⁸ with dispersion of 0.23 dex. We then randomly pick a mock luminosity from a uniform distribution between L_{lim} and $L_{\text{SFR,pred}}$ and assign it to the galaxy. Only 0.5% of the radio-undetected galaxies have $L_{\text{SFR,pred}} > L_{\text{lim}}$. For those galaxies we use L_{lim} as their mock radio luminosity. As one can see, the radio-undetected galaxies are the dominant population in the lower-left region of the AGN-SFR diagram, where RFE-off and RFI-Q galaxies co-exist. We overlay the SDSS images of low- z example galaxies ($z < 0.03$) at the corresponding grid positions in the diagram, prioritizing high-stellar-mass representatives in each cell. The images are processed with adaptive transparency to emphasize the morphology and are selected to avoid crowding.

The AI-method introduction Galaxies are divided into two groups based on their radio emission and star formation, which are labeled as Q-LERG and non-Q-LERG (Extended Data Table 1). This classification does not fully capture the nature of certain galaxies. For example, some galaxies which are influenced by radio AGNs and currently show no radio emission due to the sporadic nature of radio activity are classified as non-Q-LERG. These galaxies, referred to as RFE-off galaxies, along with the Q-LERGs, also known as RFE-on galaxies, should both be considered as RFE galaxies. Given the short duration of radio activity, RFE-off and RFE-on galaxies are expected to have similar optical properties. Conversely, the remaining non-Q-LERGs, which are fundamentally different from RFE galaxies, should be placed in the RFI category. Hence, we propose to solve the split between RFE-off and RFI galaxies by establishing a reliable RFE-galaxy classifier that can distinguish RFE and RFI galaxies. The idea behind this is that RFE-off galaxies are the intersection of RFEs (RFE-on + RFE-off) and non-Q-LERGs (RFE-off + RFI). Thus, an ideal classifier should lead to a pure extraction of RFE-off galaxies and a complete separation between RFE-off and RFI galaxies. However, the Q-LERG and non-Q-LERG annotations alone may not



Extended Data Fig. 1: The 1.4 GHz Radio luminosity-SFR relation. Panel a: The $L_{1.4\text{GHz}}$ versus SFR relation for galaxies with $\log M_*/M_\odot > 10.5$. The radio data are taken from the ref.¹². The background shows the 2D hexagon histogram of detected galaxies¹² with number indicated by the color bar. The black line shows the $L_{\text{SFR},1.4\text{GHz}}$ -SFR relation for star-forming galaxies⁴⁸. The red contours show the distribution for Q-LERGs, orange for all radio-detected galaxies, blue for radio-undetected galaxies with $L_{1.4\text{GHz}}$ being the upper-limit, and green for radio-undetected galaxies with $L_{1.4\text{GHz}}$ being a randomly assigned value between the upper-limit and the prediction based on the SFR taking into account scatter. The contour lines enclose 10%, 50%, 90% of the corresponding samples. Panel b: the same as in panel a, but shown in the same parameter space as Figure 1: $L_{1.4\text{GHz}}/L_{\text{SFR},1.4\text{GHz}}$ versus sSFR, where $L_{\text{SFR},1.4\text{GHz}}$ is the expected radio luminosity from star formation⁴⁸.

represent the radio-feedback nature of galaxies accurately, which poses a challenge to establishing a reliable RFE classifier.

To tackle this challenge, our main goal is to achieve an RFE classifier by training an AI model on the SDSS optical images with the Q-LERG/non-Q-LERG annotations. We achieve this goal by introducing an advanced noise-label learning technique commonly used in the AI community. This technique enables the AI model to learn from datasets with mislabeled entries as though it were trained on a clean dataset. Its principle is the data semantic appearance consistency. For instance, in a noisy cat-dog binary classification dataset, mislabeled dog images, whose real labels are cat, often share similar semantic appearances with most cat images, which provides cues for the AI model to recognize and correct mislabeling during training. Here, the SDSS dataset shares similar traits. “Q-LERG” and “non-Q-LERG” annotations can be seen as a noisy version of “RFE” and “RFI” labels, respectively. RFE-off galaxies can be seen as mislabeled data whose labels are “RFI” but should be “RFE”. Also, these mislabeled RFE-off galaxies are essentially RFE galaxies, so they have optical features similar to “RFE” galaxies shown in SDSS images, thus providing cues for the AI model to recognize them. Motivated by this, we utilize the symmetric cross-entropy loss function²⁶, a simple yet effective general noise-label learning method, to train our RFE galaxy classifier. This method allows the model trained on a noise dataset containing random label errors to converge statistically to the result expected from training on a clean dataset²⁶. Using such a method, our classifier learned on the SDSS dataset with the Q-LERG and non-Q-LERG labels becomes a reliable RFE galaxy classifier, which allows us to recognize RFE-off samples.

The entire pipeline of our AI method is shown in Figure 1. Each SDSS image is sent to an RFE Galaxy Classifier model to predict the probability for it to be an RFE galaxy. A Noise-Label Learning part supervises the model with Q-LERG and non-Q-LERG labels and guides it to converge to a reliable and robust RFE galaxy classifier. After the training, we treat the non-Q-LERG galaxies classified as RFE by the model as RFE-off galaxies. In the following, we introduce the details of each part of our model.

RFE Galaxy Classifier. The RFE Galaxy Classifier is formulated as a function $\hat{y} = f(x)$ where f is a model that uses x , a given SDSS image, to predict the probability, \hat{y} , for the given

image to be an RFE galaxy. We set f by Convolutional Neural Network (CNN) as follows:

$$\hat{y} = f(x) \rightarrow \hat{y} = \text{Cls}(\text{CNN}(x)), \quad (4)$$

where $\text{CNN}(\cdot)$, implemented as a ResNet50⁶¹, takes image x and returns a feature vector $h \in \mathbb{R}^C$ (C is the dimension of the feature vector) obtained by using multiple stacked convolutional layers, max-pooling layers, skip-connection operators and activation functions. The feature vector h is a low-dimensional representation of the image x which is suitable for the following classifier $\text{Cls}(\cdot)$ to predict $\hat{y} \in [0, 1]$. $\text{Cls}(\cdot)$ is implemented by a fully-connected neural network layer and a Sigmoid activation function. Obviously, the parameters of Cls and CNN determine the function of the entire AI model. The learning of the entire model is thus to adjust the parameters of Cls and CNN, and we utilize a noise-label learning technique to achieve this.

Noise-Label Learning. The learning of the RFE galaxy classifier can be defined as an optimization process and written as follows:

$$\theta^* = \arg \min_{\theta} \mathbb{E}_{(x_i, y_i) \in \mathcal{T}} \mathcal{L}(y_i, \hat{y}_i), \quad (5)$$

where x_i is the i -th sample in the the dataset \mathcal{T} while y_i and \hat{y}_i are its label and prediction, respectively. θ is the parameter set of f , specifically, the parameters of CNN and Cls. \mathcal{L} is the loss function that measures the gap between the predicted probability \hat{y} and the corresponding ground-truth label y . The final goal is to find an optimized parameter set θ^* which can minimize of the expected value of the loss function. Here, we use the Symmetric Cross-Entropy loss function²⁶ for \mathcal{L} . The detailed formulation is as follows:

$$\mathcal{L}(y, \hat{y}) = \underbrace{-y \cdot \log(\hat{y}) - (1 - y) \cdot \log(1 - \hat{y})}_{\text{Cross-Entropy term}} \underbrace{-\hat{y} \cdot \log(y) - (1 - \hat{y}) \cdot \log(1 - y)}_{\text{Reverse Cross-Entropy term}}. \quad (6)$$

The entire loss function has two terms, a Cross-Entropy (CE) term and a Reverse Cross-Entropy (RCE) term. The CE term is used to constrain the model to adapt \hat{y} as close to y as possible, which guides the model to learn correlations between input image x and label y . The RCE term is a noise-robust learning term, which can make the entire model converge to the same optimized results as it was trained on a clean dataset with the cross-entropy loss function. This term thus allows the model to ignore the impact of noise labels in the training data²⁶ and give a reliable RFE galaxy classifier.

PK-Sampling for balanced training. The Q-LERGs and non-Q-LERGs exhibit a severe class imbalance, with 3,095 positive samples (Q-LERGs) and 397,214 negative samples (non-Q-LERGs). Direct training on this imbalanced dataset would result in a trivial classifier biased toward the majority class (i.e., predicting negative universally). To address this, we implement the PK-sampling strategy ⁶², which constructs balanced epoch data by sampling an identical quantity of positive (Q-LERG) and negative (non-Q-LERG) samples per training iteration. Specifically, each training epoch comprises a balanced subset formed by all positive samples and an equal-sized randomly sampled subset of negative samples. Upon completing an epoch, the negative samples are re-sampled to form a new balanced subset for the next epoch. This process repeats for 50 epochs, ensuring the model 1) to be exposed to most available data while 2) to be able to mitigate the bias induced by class imbalance.

Data Augmentation. Data augmentation is a widely adopted technique in machine learning to improve model generalization and robustness. In our training pipeline, we employed the following augmentation strategies:

- **Color Jitter:** With a 50% probability, we applied random perturbations to image brightness and contrast to simulate varying lighting conditions. This enhanced color diversity and mitigated overfitting to specific color distributions.
- **Random Flip:** Each image had a 50% chance of being flipped either horizontally or vertically, encouraging the model to learn flip-invariant features.
- **Random Rotation:** Each image was randomly rotated with a 50% probability, introducing rotational invariance into the learned representations.
- **Random Erasing:** With a 50% probability, a randomly selected region of the image was erased. This encouraged the model to rely on holistic spatial features rather than overfitting to specific discriminative regions ²⁵.

Model Inference. After training the model, for a sample x , the trained model can provide \hat{y} to indicate the probability of x belonging to a radio galaxy. We set a threshold th to transfer the

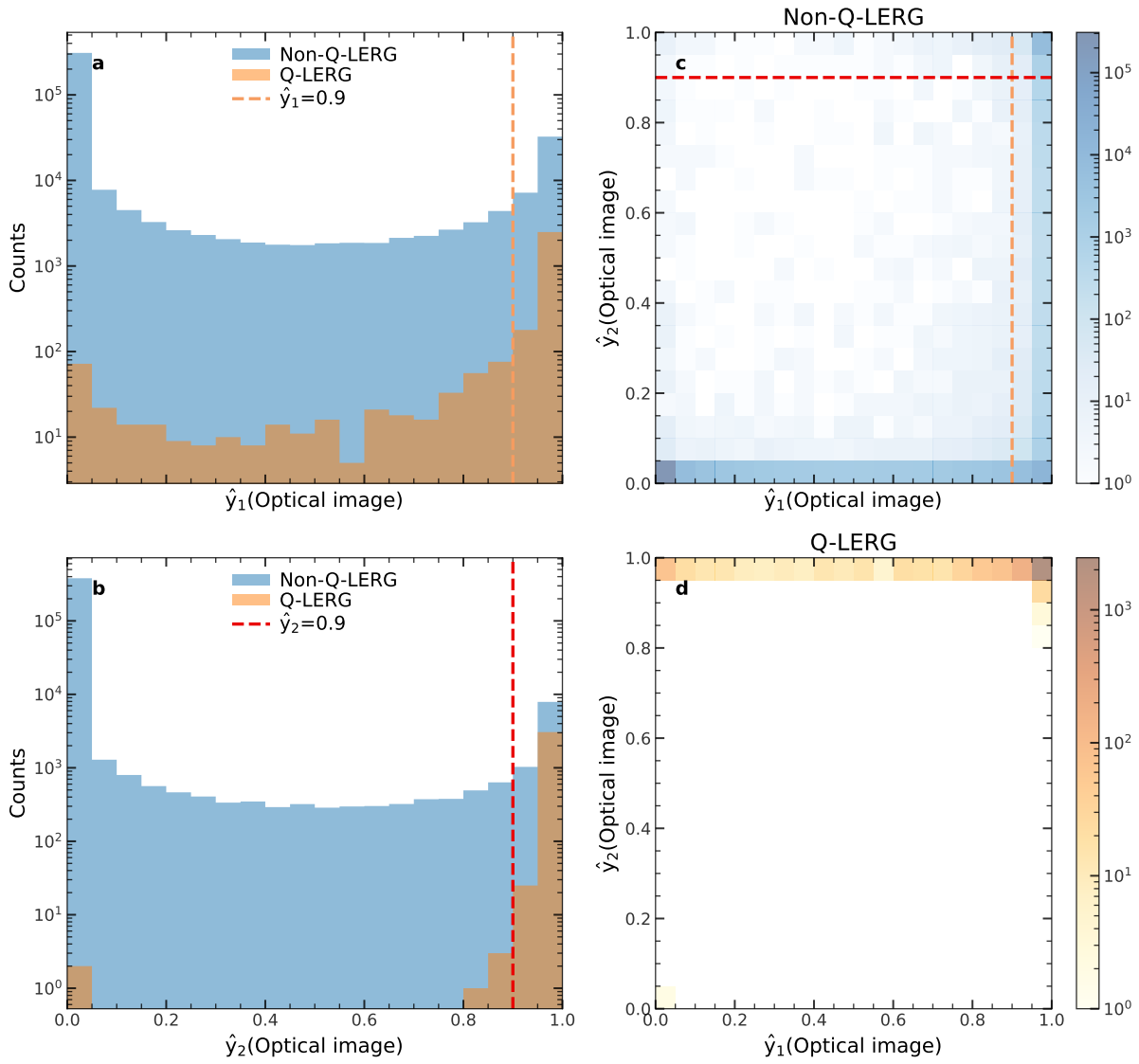
predicted continuous probability \hat{y} into discrete classes as follows:

$$c = \begin{cases} 1 & \text{if } \hat{y} \geq th, \\ 0 & \text{if } \hat{y} < th, \end{cases} \quad (7)$$

where c is the final predicted class and th is a threshold. In the next section, we will show the choice of th and the classification result.

AI classification of RFE and RFI galaxies We applied our AI technique to the optical images to compute \hat{y}_1 (with data augmentation) and \hat{y}_2 (without data augmentation) for each galaxy. Extended Data Fig. 2 illustrates the distributions of \hat{y}_1 and \hat{y}_2 for Q-LERGs and non-Q-LERGs, respectively. Most Q-LERGs have both \hat{y}_1 and \hat{y}_2 close to 1, indicating that they share the same features. Therefore, all Q-LERGs are treated as RFE-on galaxies. The \hat{y}_1 and \hat{y}_2 distributions for non-Q-LERGs have two distinct peaks at 0 and 1, respectively. This suggests that part of the non-Q-LERGs are very similar to Q-LERGs, while others are markedly different. Considering that most Q-LERGs exhibit \hat{y}_1 and \hat{y}_2 values exceeding 0.9, we opted to set $th = 0.9$ as the threshold to identify RFE-off galaxies from non-Q-LERGs. Our tests reveal that variation in th from 0.2 to 0.9 has negligible impact on our results. This is anticipated because \hat{y}_1 and \hat{y}_2 for most galaxies are close to either one or zero. Divergences between \hat{y}_1 and \hat{y}_2 occasionally occur (Extended Data Fig. 2), highlighting the difficulty in classifying RFE and RFI galaxies solely based on noise labels. Consequently, we implemented a two-tier classification process. The results are listed in Extended Data Table 2. Initially, we used $\hat{y}_1 = 0.9$ to divide non-Q-LERGs into two categories. Non-Q-LERGs with $\hat{y}_1 < 0.9$ are designated as the RFI sample, while those with $\hat{y}_1 \geq 0.9$ form the RFE-off sample with high completeness (cRFE-off). A total of 918 star-forming galaxies (0.4% of the total population) have $\hat{y}_1 \geq 0.9$, but are actually classified as RFI galaxies. Subsequently, a pure RFE-off (pRFE-off) sample was derived from the cRFE-off sample by imposing an additional requirement of $\hat{y}_2 \geq 0.9$. Thus, the pRFE-off sample constitutes a subset of the cRFE-off sample. The pRFE sample is derived by merging the RFE-on and pRFE-off samples, whereas the cRFE sample is formed by combining the RFE-on and cRFE-off samples. The galaxy numbers of these samples are listed in Extended Data Table 1.

Extended Data Fig. 3 displays images of randomly chosen from RFE-on, pRFE-off, cRFE-off, RFI-Q, or RFI-SF at $z < 0.04$ and with $\log M_*/M_\odot > 10.5$. RFE galaxies appear red,



Extended Data Fig. 2: Distributions of \hat{y}_1 and \hat{y}_2 . Panel a,b: the number count histograms of \hat{y}_1 and \hat{y}_2 for Q-LERGs (orange) and non-Q-LERGs (blue). The dashed lines show the threshold of 0.9. Panel c,d: the 2D histograms of galaxy number. The parameter \hat{y}_1 and \hat{y}_2 are calculated by our AI technique based on the optical SDSS image with and without data augmentation, respectively. The parameters are used to evaluate the similarity between the images of unclassified galaxies and RFE-on galaxies. Large \hat{y} means that the galaxies are similar to the RFE-on galaxies (see Methods).



Extended Data Fig. 3: Optical images for different types of galaxies. Panel a-d: the randomly selected images for RFE-on galaxies in four mass bins. Panel e-h: pRFE galaxies. Panel i-l: cRFE galaxies. Panel m-p: RFI-Q galaxies. Panel q-t: RFI-SF galaxies. The shown galaxies are selected from those at $z < 0.04$ and with $\log M_\star / M_\odot > 10.5$. The stellar masses, sSFR, \hat{y}_1 and \hat{y}_2 are shown in each panel.

smooth, and spherical. RFI-Q galaxies tend to be slightly bluer and more elongated compared to RFE galaxies. RFI-SF galaxies are usually blue, and some of them exhibit spiral arms. These are consistent with the results shown in Figure 3.

What AI learns To understand what information the AI technique acquires, we conducted four additional experiments in which the training utilized only portions of the image instead of the entire image for each galaxy. The initial two experiments focused on the peripheral regions beyond the radii of $0.75R_{50}$ and $1.5R_{50}$, respectively, which are referred to as P1 and P2. The latter two experiments were limited to the central areas of each image, confined within the radii of $0.75R_{50}$ and $1.5R_{50}$, respectively. The two experiments are referred to as C1 and C2, respectively. The results of these experiments are summarized in Extended Data Table 2. Both the P1 and P2 experiments obtain results similar to those of the full image training, while there are many more non-Q-LERGs in C1 and C2 that have $\hat{y}_1 \geq 0.9$. These tests demonstrate that the galaxy outskirts are more crucial for the classification of RFE and RFI than the inner regions. It is consistent with the results shown in Figure 3.

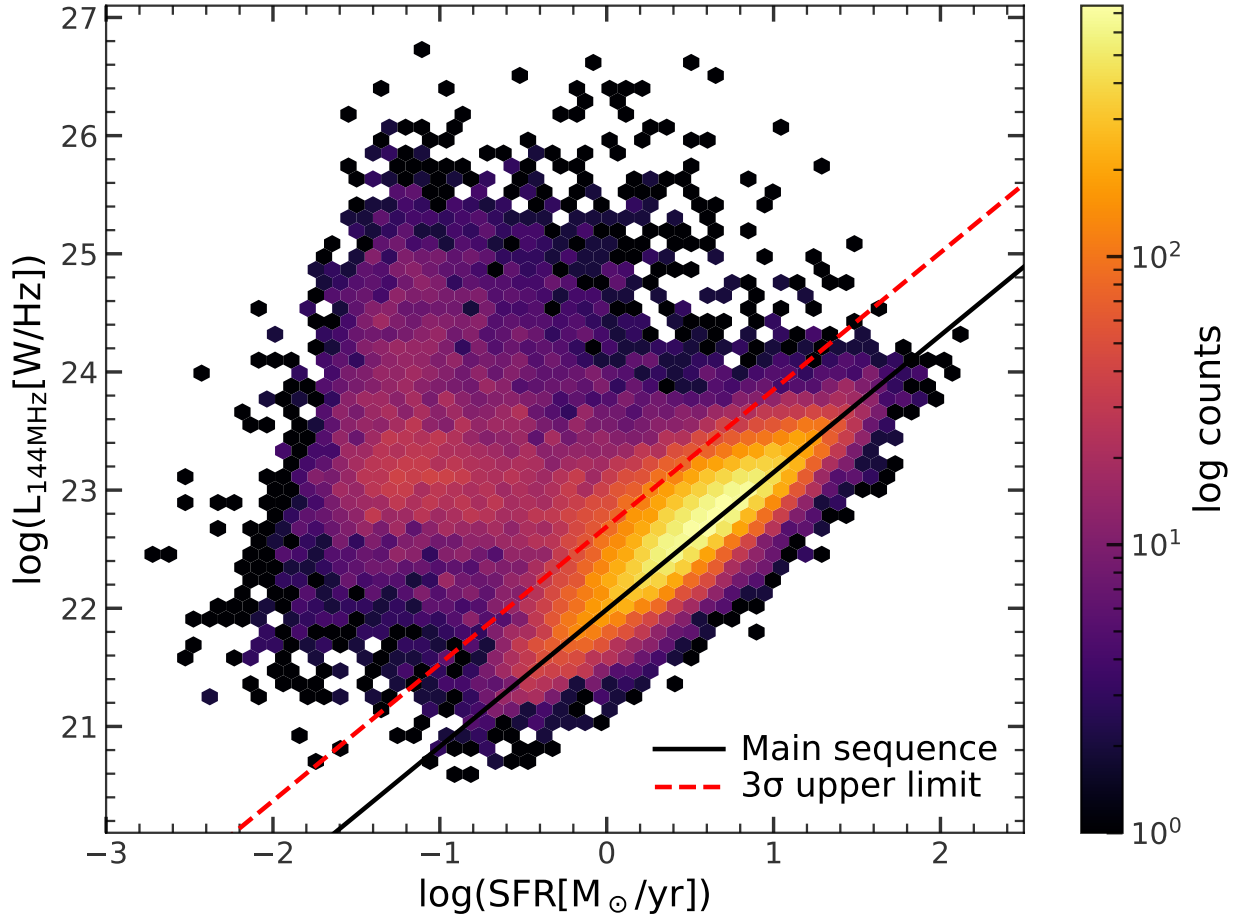
Completeness and purity The performance of a classification method is usually assessed by two metrics, completeness and purity. In this section, we evaluate the two metrics for RFE-off galaxies. Completeness refers to the proportion of intrinsic RFE-off galaxies that are correctly classified, while purity refers to the proportion of galaxies classified as RFE-off galaxies that are intrinsically RFE-off galaxies. A standard approach to assess the two parameters is to apply the method to a test sample, within which galaxies have been accurately classified by an independent and reliable method. However, there are no well-defined RFE-off sample in the literature, because RFE-off and RFI-Q galaxies occupy the same region in the AGN-SF diagram (Figure 1). Therefore, we need an alternative method.

To evaluate the completeness, we randomly selected 90% of Q-LERGs (RFE-on) for training purposes. We then applied the trained AI to the rest 10% Q-LERGs which are treated as intrinsic RFE-off galaxies in the test. The approach is reasonable because RFE-off galaxies have optical images similar to those of RFE-on galaxies. We conducted 10 such tests with randomly selected test galaxies. The completeness is calculated as $C = N_{s,QL}/N_{t,QL}$, where $N_{t,QL}$ is the number of test Q-LERGs and $N_{s,QL}$ is the number of test Q-LERGs classified as RFE galaxies.

Extended Data Table 2: Numbers of galaxies in different classes based on the AI classification

Initial label	Q-LERGs		non-Q-LERGs	
Full image	$\hat{y}_1 > 0.9$	$\hat{y}_1 \leq 0.9$	$\hat{y}_1 > 0.9$	$\hat{y}_1 \leq 0.9$
$\hat{y}_2 > 0.9$	2668	421	8786	139
$\hat{y}_2 \leq 0.9$	4	2	30916	357373
P1($> 0.75R_{50}$)	$\hat{y}_1 > 0.9$	$\hat{y}_1 \leq 0.9$	$\hat{y}_1 > 0.9$	$\hat{y}_1 \leq 0.9$
$\hat{y}_2 > 0.9$	2668	423	7705(70.9%)	122
$\hat{y}_2 \leq 0.9$	3	1	32148(79.6%)	357239
P2($> 1.5R_{50}$)	$\hat{y}_1 > 0.9$	$\hat{y}_1 \leq 0.9$	$\hat{y}_1 > 0.9$	$\hat{y}_1 \leq 0.9$
$\hat{y}_2 > 0.9$	2631	463	8058(69.4%)	115
$\hat{y}_2 \leq 0.9$	1	0	31090(76.8%)	357951
C1($< 0.75R_{50}$)	$\hat{y}_1 > 0.9$	$\hat{y}_1 \leq 0.9$	$\hat{y}_1 > 0.9$	$\hat{y}_1 \leq 0.9$
$\hat{y}_2 > 0.9$	2560	288	32774(24.2%)	6245
$\hat{y}_2 \leq 0.9$	55	192	15715(32.4%)	342480
C2($< 1.5R_{50}$)	$\hat{y}_1 > 0.9$	$\hat{y}_1 \leq 0.9$	$\hat{y}_1 > 0.9$	$\hat{y}_1 \leq 0.9$
$\hat{y}_2 > 0.9$	2661	346	21218(35.1%)	1746
$\hat{y}_2 \leq 0.9$	28	60	24999(52.8%)	349251

The table shows the numbers of galaxies in different categories based on AI classification parameters \hat{y}_1 and \hat{y}_2 . The “Full image” run is the fiducial run and uses the whole image of each galaxy for the training. The P1, P2, C1 and C2 runs use only part of each image(as indicated after the name) for the training (see Methods). Percentages shown in the fourth column indicate the fraction of galaxies in each (\hat{y}_1, \hat{y}_2) category trained with partial images (P1, P2, C1, C2) that are also classified into the same (\hat{y}_1, \hat{y}_2) category by the fiducial run. High percentage means that the corresponding run obtains result similar to that of the fiducial run.



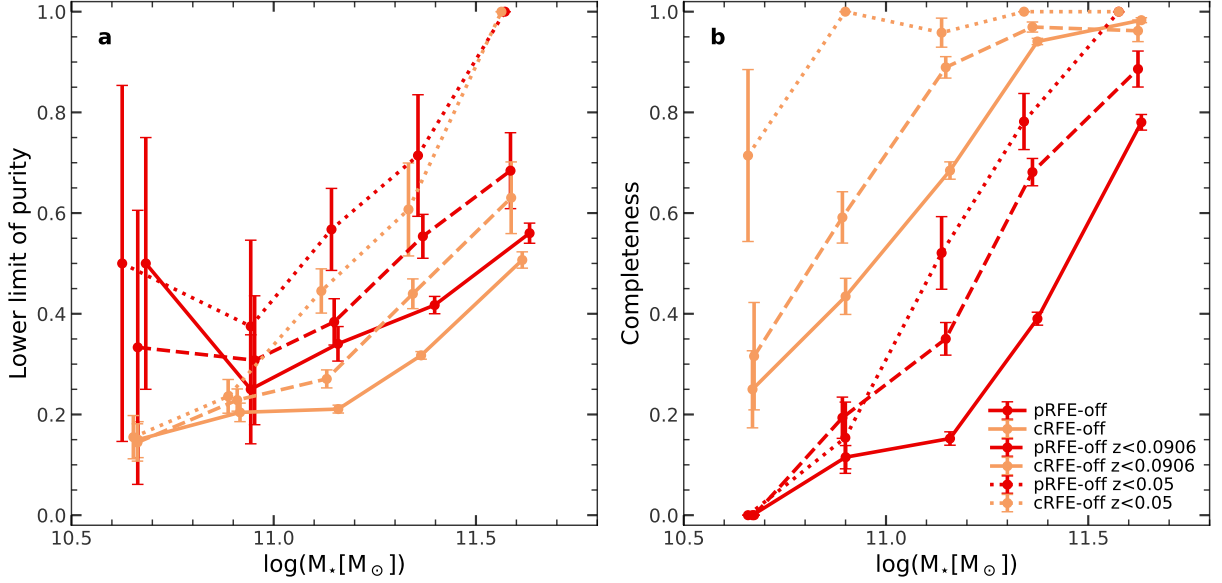
Extended Data Fig. 4: Distribution of LOTSS DR2 galaxies in L-SFR plane. The background shows a 2D histogram (hexbin) of galaxy number as indicated by the color bar. The solid black line indicates the star-forming main sequence ($L_{\text{SFR},144\text{MHz}}\text{-SFR}$ relation)⁶³, while the dashed red line shows the relation plus 3σ , where $\sigma = 0.2$ dex is the scatter of the relation.

The purity of RFE-off samples is estimated using a deeper radio survey, the LOFAR Two-Metre Sky Survey (LOTSS) DR2⁶⁴, observed at a central frequency of 144 MHz. LOTSS DR2 covers about 5700 deg² in the northern sky. We selected a regular region with right ascension between 150° and 230°, and declination between 30° and 65°, which is located within the SDSS regions. A total of 33,932 of our galaxies are detected and 56,234 are not. Extended Data Fig. 4 shows the radio luminosity, $L_{144\text{MHz}}$, versus SFR for the detected galaxies. Consistent with our main radio sample (Extended Data Fig. 1), there are two populations. The first population has $L_{144\text{MHz}}$ closely correlated with SFR, following well the $L_{\text{SFR},144\text{MHz}}$ -SFR relation for star-forming galaxies⁶³, indicative of the star-formation origin of the radio luminosity. The other population lies above the star-forming main sequence. The excess radio luminosity originates from radio AGNs. Following the ref.⁶³, we selected radio-excess galaxies using

$$\log(L_{144\text{MHz}}[\text{W/Hz}]) \geq L_{\text{SFR},144\text{MHz}} + 3\sigma_L = 21.99 + 1.16 \log(\text{SFR}[M_\odot/\text{yr}]) + 0.7, \quad (8)$$

where $L_{\text{SFR},144\text{MHz}}$ is the $L_{144\text{MHz}}$ -SFR relation for star-forming galaxies (Extended Data Fig. 4) and $\sigma_L = 0.23$ is the scatter of the relation⁶³. We assume that a galaxy exhibiting radio excess and yet classified as RFE-off represents an intrinsic RFE-off galaxy, undetectable by the NVSS/FIRST survey but discernible through the LOTSS survey. This galaxy is likely experiencing low-level activity within its duty cycle. The low-limit of the purity is defined by $P_{\text{ll}} = N_{\text{off, re}}/N_{\text{off}}$, where N_{off} corresponds to the count of RFE-off galaxies within the selected sky region, and $N_{\text{off, re}}$ denotes the number of RFE-off galaxies manifesting radio excess at 144MHz. P_{ll} serves as a low-limit due to the fact that some intrinsic RFE-off galaxies possess radio activity too faint for LOTSS detection.

The completeness of the cRFE-off and pRFE-off samples is 85.0% and 40.2%, respectively. The average P_{ll} for pRFE-off galaxies stands at 46%, significantly surpassing that of cRFE-off galaxies at 29.5%. Extended Data Fig. 5 shows C and P_{ll} as functions of M_\star . The two metrics for both cRFE and pRFE increase strongly with increasing M_\star , indicative of the low efficiency of the method at the low-mass end. We also assessed the two metrics for galaxies at $z < 0.0906$, where radio galaxies with $L_{1.4\text{GHz}} > 10^{23} \text{ WHz}^{-1}$ are complete and galaxies with $\log M_\star/M_\odot > 10.5$ are also nearly complete. This sample can be used to estimate the RFE fraction and duty cycle (Figure 2). The mean C for pRFE-off and cRFE-off samples are 52% and 87%, respectively. The mean P_{ll} for pRFE-off and cRFE-off samples are 49% and 30%, respectively. We also assessed



Extended Data Fig. 5: Completeness and purity. Panel a: the lower limit of purity as a function of M_* . The red lines show the results for pRFE-off sample, and the orange lines show the results for cRFE-off sample. The solid lines show the results using all galaxies with $z < 0.2$, dotted line for galaxies with $z < 0.0906$ and dashed lines for galaxies with $z < 0.05$. Panel b: the completeness as a function of M_* . The completeness, estimated using a standard 90/10 train-test split of the data. There is only 34 Q-LERGs (at $z < 0.2$) in the lowest M_* bin, leading to large uncertainties in completeness. Purity refers to the fraction of selected RFE-off galaxies that are observationally confirmed in LOTSS, a deeper low-frequency radio survey catalog⁶⁴. See Methods for details. Error bars represent Poisson 1σ uncertainties.

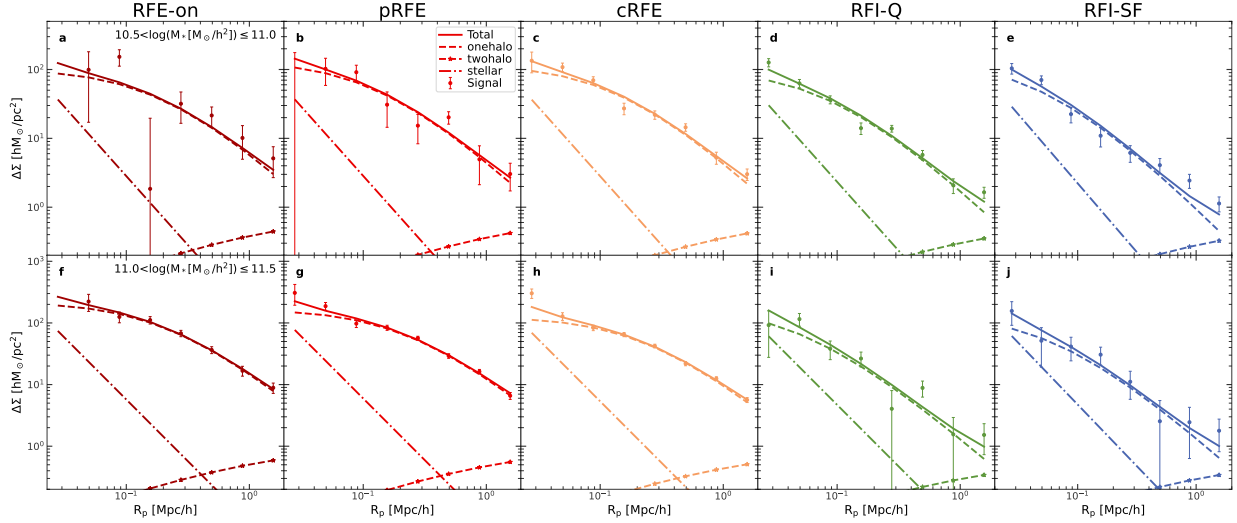
the two metrics for galaxies at $z < 0.05$, which is the redshift range for xGASS galaxies. The mean C for pRFE-off and cRFE-off samples are 55% and 97%, respectively. The mean P_{11} for pRFE-off and cRFE-off samples are 60% and 32%, respectively. The two metrics can be used to estimate the RFE fraction in gas-poor galaxies (Figure 2). As can be seen, both metrics improve as the redshift decreases. One possible reason for the improvement is that galaxies at lower redshift have images of better quality. In the future, our method can be applied to the higher-quality images of the upcoming WFST survey⁶⁵ to improve performance.

Spatially resolved MaNGA data The SDSS Mapping Nearby Galaxies at Apache Point Observatory (MaNGA)²⁸ data release 17 provides spatially resolved spectra of about 10,000 galaxies in the SDSS region⁶⁶. We adopted the data product of Pip3D⁶⁷, which provides the measurement of stellar velocity dispersion (σ_*) and the 4000Å break (D4000) on each spaxel. Following our previous study³⁰, we calculated the inner stellar velocity dispersion (σ_{in}), outer stellar velocity dispersion (σ_{out}), inner D4000 ($D4000_{in}$) and outer D4000 ($D4000_{out}$). The two inner parameters are the median values of the spaxels within the inner $0.2R_{50}$ elliptical annuli, and the two outer parameters are the median within the $1.4-1.5R_{50}$ elliptical annuli. The position angle and ellipticity that determine the elliptical annuli are taken from the NSA catalog⁶⁸. To obtain reliable measurements of these quantities, we exclude spaxels with a signal-to-noise ratio of σ_* less than 3. After cross-matching with our central galaxy sample, we have total 5,462 galaxies. Among 2,789 galaxies with $\log M_*/M_\odot > 10.5$, there are 140 RFE-on galaxies, 679 pRFE galaxies, 1,249 cRFE galaxies, 601 RFI-Q galaxies and 939 RFI-SF galaxies.

Figure 3 shows the distributions of these parameters for the MaNGA galaxies with $11.0 < \log M_*/M_\odot < 11.5$. Note that the two dynamical parameters are scaled with $\sigma_{hot}(M_*)$, which is the scaling relation of dynamical hotness and is taken from our previous study³⁰. A region is considered dynamically hot when its velocity dispersion is comparable to $\sigma_{hot}(M_*)$. RFE-on and RFE galaxies exhibit very similar spatially-resolved properties. The distinctions between RFE and RFI galaxies, including the quenched ones, are quite pronounced. The differences in the outskirts are larger than those in the central regions. RFI-Q galaxies generally have a colder and younger stellar component in the outskirts compared to RFE galaxies. This result is consistent with that the AI technique differentiates RFE and RFI galaxies primarily based on the outskirt image.

Weak lensing measured halo mass The shear catalog used for measuring weak lensing signals is constructed from the Dark Energy Camera Legacy Survey (DECaLS) Data Release 8 (DR8) imaging data^{69,70}. The shape of each galaxy is measured using the FOURIER_QUAD pipeline, which has been demonstrated to provide accurate shear measurements even for extremely faint galaxy images with signal-to-noise ratios (SNR) below 10^{32,71–73}. The shear catalog spans over ten thousand square degrees in the g , r , and z bands, containing approximately 99, 111, and 116 million distinct galaxies in each band, respectively. We note that the images of the same galaxy on different exposures are counted as different images in the FOURIER_QUAD method. In this work, we only use the r and z band data. The DECaLS region overlapped with SDSS DR7 is 4744 square degrees, corresponding to approximately 68% of the SDSS survey area. The estimator, Excess Surface Density (ESD) $\Delta\Sigma(R) = \gamma_t(R)\Sigma_{\text{crit}}$ is measured using the PDF-Symmetrization method⁷⁴, which minimizes the statistical uncertainty. Extended Data Fig. 6 shows the ESD for RFE-on, pRFE, cRFE, RFI-Q and RFI-SF galaxies in two overlap M_* bins. The error bars are estimated using 150 bootstrap samples.

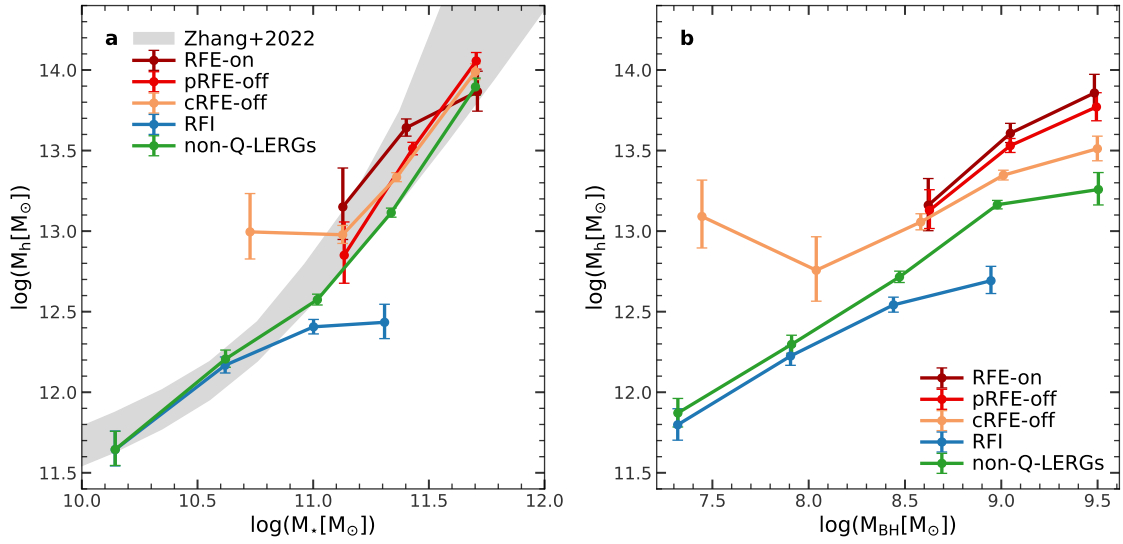
Following previous studies^{42,75,76}, the ESD is modeled using three components, $\Delta\Sigma = \Delta\Sigma_{\text{stellar}} + \Delta\Sigma_{\text{NFW}} + \Delta\Sigma_{2\text{h}}$ (Extended Data Fig. 6). The first term is the contribution from the stellar mass of the central galaxies, which is modeled as a point mass. The second term is the contribution of the dark matter halo with a Navarro-Frenk-White⁷⁷ density profile, which has two free parameters, mass m_h and concentration c . Here, m_h is the mass contained in the spherical region of radius $r_{200\text{m}}$, where the mean mass density is equal to 200 times the mean matter density of the Universe. Following previous study⁷⁵, we do not consider the off-centering effect, which is negligible according to our tests. The third term is the two-halo term which was calculated by projecting along the line-of-sight of the halo-matter cross-correlation function ξ_{hm} , where $\xi_{\text{hm}} = b(m_h)\xi_{\text{mm}}$. Here ξ_{mm} is the linear matter-matter correlation function and $b(m_h)$ is the linear halo bias⁷⁸, these two are generated from *COLOSSUS*. We sample the posterior distributions of the two parameters, m_h and c , using Markov Chain Monte Carlo (MCMC) with a software *emcee*⁷⁹. Both *COLOSSUS* and *emcee* are under the MIT License. The best-fitting profiles are presented in Extended Data Fig. 6. The quoted mass, m_h , is the median value of the posterior and its error bars indicate the 16 and 84 percentiles of the posterior. We note that m_h actually accounts for the contribution of cold dark matter, diffuse gas, and satellites around the centrals but does not include the contribution of



Extended Data Fig. 6: Excess surface density from DECaLS and best fitting. The symbols show the excess surface density (ESD) profiles obtained by stacking the lensing signal. Panel a-e: the results for galaxies with $10.5 \leq \log M_*/M_\odot \leq 11.0$ in RFE-on, pRFE, cRFE, RFI-Q and RFI-SF samples, respectively. Panel f-j: the results for galaxies with $11.0 \leq \log M_*/M_\odot \leq 11.5$. The shear catalog we used is constructed from the DECaLS DR8 imaging data. The error bars correspond to the standard deviation of 150 bootstrap samples. We fit the ESD by using three components, stellar mass term (dash-dotted lines), one-halo term (dashed lines), and two-halo term (dotted lines with stars). The total fitting results are indicated by the solid lines.

central galaxies, which are modeled separately. So, the total mass of the halo should include all components within the virial radius of the halo, is $M_h = m_h + M_*$. Usually, $M_* \ll m_h$, so M_h is very close to m_h . In this paper, when we talk about halo mass, what we mean specifically is the total mass of the halo, i.e. M_h .

In Extended Data Fig. 7, we show M_h as function of M_* and M_{BH} for Q-LERGs and non-Q-LERGs. Consistent with previous study³¹, the M_h difference between the two populations at given M_* is about 0.3 dex. For comparison, we also present the results for pRFE-off, cRFE-off and RFI galaxies. Similar to that in Figure 3, the difference between RFE and RFI galaxies is very large. Apparently, the non-Q-LERG sample comprises two distinct populations, RFI and RFE-off galaxies. RFE-off galaxies reside in massive halos, comparable to those of Q-LERGs, while the host halos of RFI galaxies are much smaller.



Extended Data Fig. 7: Stellar mass-Halo mass relation and Black hole mass-Halo mass relation. Panel a: M_*-M_h relation for different populations. The grey shaded region represents the empirical relation from the ref.⁴². Panel b: $M_{BH}-M_h$ relation. The halo masses are estimated by using weak lensing technique. We only show the results for bins with error less than 0.5 dex and galaxy numbers above 100. The error bars represent the 16th–84th percentiles of 150 bootstrap samples.

HI data from xGASS survey The HI results shown in Figure 4 are based on HI data sourced from xGASS representative sample provided by the Galaxy Evolution Explorer Arcibo SDSS Survey³⁶. The xGASS representative sample includes randomly-selected galaxies from the parent sample of objects in the SDSS DR7 spectroscopic catalog, located within the footprint of the Arcibo Legacy Fast ALFA (ALFALFA) survey⁸⁰. They are uniformly selected across the stellar mass range of $9 < \log(M_*/M_\odot) < 11.5$. These galaxies have been observed at 21cm by Arcibo until HI was detected or until an upper limit of a few percent in gas fraction (M_{HI}/M_*) was reached. Since most RFE galaxies have $\log M_*/M_\odot > 10.5$, our analysis is restricted to galaxies above this mass limit. By cross-matching our central galaxy sample and xGASS representative sample, we selected 323 galaxies that have xGASS HI data, with a redshift range of $0.01 \leq z \leq 0.05$ and $\log(M_*/M_\odot) \geq 10.5$. Among these galaxies, 130 have only an upper limit for the gas fraction.

There are 6 RFE-on galaxies, 42 pRFE galaxies, 106 cRFE galaxies, 101 RFI-Q galaxies and 116 RFI-SF galaxies. Figure 4 illustrates that RFI-Q galaxies exhibit a considerably higher gas fraction compared to RFE galaxies. It is known that the gas fraction depends on M_* , and the M_* distributions for RFI-Q and RFE galaxies differ (Figure 3). To address this mass dependency, we constructed M_* -controlled RFI-Q samples, which has M_* distribution similar to that of cRFE or pRFE sample. For each galaxy in pRFE (cRFE) sample, a matched galaxy is randomly chosen from the RFI-Q sample with a mass difference of < 0.1 dex. 1000 control samples are created. The distributions of gas-rich fraction for these control samples are shown in Figure 4. We also constructed control RFI-Q samples with M_{BH} or NUV-r color controlled. The tolerances are $\Delta \log M_{\text{BH}}/M_\odot < 0.3$ and $\Delta(\text{NUV} - r) < 0.3$, respectively. Note that if there is no matched galaxy within the tolerance, a galaxy with the smallest difference in the property considered is selected. The gas-rich fractions for these control samples are presented in Figure 4. As one can see, RFE galaxies are apparently gas poor compared to RFI-Q galaxies even after the galaxy properties are controlled. We also constructed control RFI-Q samples with both NUV-r and stellar surface density controlled. The results are similar to those with NUV-r controlled and thus not presented here.

Galaxy fractions Figure 2 shows the fraction of different galaxies. Here we present the methods to calculate these fractions. For a given RFE (cRFE or pRFE) sample, we calculated the fraction

of RFE galaxies as

$$f_{\text{RFE}} = \frac{N_{\text{off}} * P/C + N_{\text{on}}}{N_{\text{all}}}, \quad (9)$$

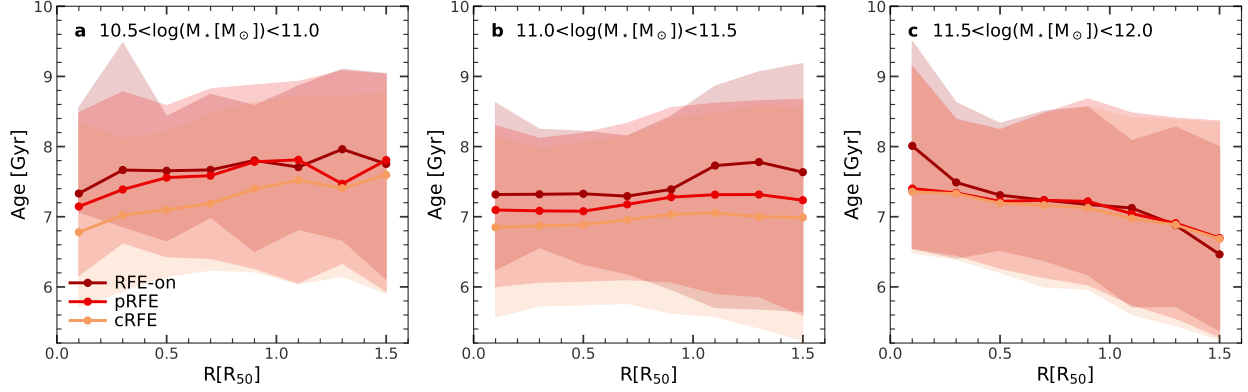
where N_{all} is the number of galaxies in the total sample, N_{on} and N_{off} are the numbers of RFE-on and RFE-off galaxies in the RFE sample, respectively, and P and C are the purity and completeness of the RFE-off sample. The fraction of quenched galaxies is $f_{\text{q}} = \frac{N_{\text{q}}}{N_{\text{all}}}$, where N_{q} is the number of quenched galaxies. Figure 2 shows these fractions as functions of M_{\star} . Since it is difficult to measure a precise value of P , we present the results with $P = P_{\text{ll}}$ and $P = 1$ in the figure. The RFE fractions increase rapidly with M_{\star} , while the quenched fraction increases gradually with M_{\star} . It is evident that the quenched fraction is significantly larger than the RFE fraction for $\log M_{\star}/M_{\odot} < 11.5$. This indicates that the radio feedback is not the major mechanism for the massive quenched galaxies with $\log M_{\star}/M_{\odot} < 11.5$ to maintain their quiescence.

Duty cycle Radio galaxies are known to experience cycles of activity and silence. We calculated the duty cycle fraction as,

$$f_{\text{dc}} = \frac{N(> L_{\text{th}})}{N_{\text{on}} + N_{\text{off}} * P/C}, \quad (10)$$

where $N(> L_{\text{th}})$ is the number of RFE galaxies with radio luminosity above L_{th} , N_{on} is the number of RFE-on galaxies, N_{off} is the number of RFE-off galaxies, and P and C are the purity and completeness of the sample. Note that the denominator is actually the intrinsic number of RFE galaxies. Since most RFE-on galaxies have $L_{1.4\text{GHz}} > 10^{23} \text{W Hz}^{-1}$, we set $L_{\text{th}} = 10^{23} \text{W Hz}^{-1}$. Given the flux limit of 5 mJy, radio galaxies above this threshold are complete at $z < 0.0906$. The completeness and purity at this redshift range are shown in Extended Data Fig. 5. For comparison, we also estimated the duty cycle fraction using a traditional approach, defined as the fraction of Q-LERGs ($L_{1.4\text{GHz}} > 10^{23} \text{W Hz}^{-1}$) among all galaxies. The results are shown in Figure 2c. Note that galaxies with $\log M_{\star}/M_{\odot} > 10.5$ are also complete in this redshift range. We emphasize that the duty cycle fraction is impossible to estimate if we do not have a reasonable estimation for the number of intrinsic RFE galaxies.

To convert the duty cycle fraction into physical time durations, we assume a total RFE timescale of $t_{\text{RFE}} = 7.2 \text{ Gyr}$, motivated by the stellar population properties of RFE galaxies with $\log M_{\star}/M_{\odot} > 10.5$ in the MaNGA survey^{28,81}. As shown in Extended Data Fig. 8, the stellar age radial profiles of these RFE galaxies show little dependence on radius, with a median



Extended Data Fig. 8: Stellar age radial profile from MaNGA The x-axis shows radius normalized by the effective radius R_{50} , and the y-axis represents the mass-weighted stellar age in Gyr. Shaded regions show the 16th–84th percentile range.

mass-weighted stellar age of approximately 7.2 ± 1.1 Gyr. We then adopt $t_{\text{RFE}} = 7.2$ Gyr as a representative timescale for the maintenance of quenching by radio feedback. The on-duty duration is then calculated as

$$t_{\text{on}} = f_{\text{dc}} t_{\text{RFE}}. \quad (11)$$

The corresponding off-duty time is $t_{\text{off}} = t_{\text{RFE}} - t_{\text{on}}$. Figure 2c and d show t_{on} and t_{off} as functions of M_* . Previous studies²⁷ derived the duration of a single radio AGN activity as a function of M_* ,

$$t_{\text{on,single}} = 4.8 \text{ Myr } f^{-1/2} (M_*/M_{\odot})^{0.7} \quad (12)$$

where f is a scaling factor in their jet power–luminosity relation, for which we adopt $f = 5$. Interestingly, the slope of the $t_{\text{on,single}} - M_*$ relation is similar to our $t_{\text{on}} - M_*$ relation. We scaled the $t_{\text{on,single}} - M_*$ relation by 300 and found that it matches our result very well (blue dashed line in Figure 2). This suggests that on average an RFE galaxy has experienced around 300 cycles.

Misalignment between HI gas and stellar kinematics The kinematic properties and morphology of the HI gas can help us to understand the origin of the cold gas in quenched galaxies. If the HI gas is accreted after the host galaxies are quenched, it is expected that the HI gas will exhibit irregularities or a kinematic misalignment with the stellar component. The ATLAS^{3D} HI survey⁸ presented a HI survey of a volume-limited sample of 166 local early-type ATLAS^{3D} galaxies. Each galaxy was observed for 12 hours using the Westerbork Synthesis Radio Telescope (WSRT). Of 166 galaxies, 53 galaxies are detected. The stellar masses of these galaxies are calculated based

on their K-band luminosities using the method presented in the ref.⁸². We adopted the SFRs⁸³ estimated by fitting the infrared SED from AKARI, WISE and 2MASS. The SFR for NGC 2594 is taken from another catalog⁸⁴. A large fraction of these galaxies are satellite galaxies located within massive groups and clusters, such as the Virgo cluster⁸. Therefore, the HI gas of certain RFI-Q galaxies may be removed by environmental effects. We thus selected gas-rich quiescent galaxies, for which the environmental effect is expected to be weak, to represent RFI-Q galaxies. Only seven galaxies are quenched ($\log sSFR < -11$) and possess a substantial amount of HI gas ($\log M_{\text{HI}}/M_{\star} > -1.5$). These galaxies include NGC 6798, NGC 2594, NGC 2685, NGC 5173, UCG 09519, NGC 5582 and NGC 3073. Among them, NGC 6798, NGC 2685 and NGC 5582 were observed with WSRT for 108 hours per galaxy in follow-up observations. Recently, Yang et al.⁴⁰ performed a detailed dynamical modeling on the stellar component and the HI gas for these galaxies and found that their HI velocity fields can be well fitted by rotational velocity fields. We thus adopted the kinematic data provided by Serra et al. and Yang et al. Serra et al. identified distinct signs of misalignment between the rotational axes of HI gas and stellar components in the first five galaxies. In the last one, complex morphology and unsettled kinematics for HI gas was noted. Yang et al. corroborated these findings, and, intriguingly, their detailed modeling also detected a considerable misalignment in NGC 5528. Thus, among the seven galaxies, five show evident misalignment signals, one presents an irregular morphology, and one remains uncertain, supporting that the HI gas in the RFI-Q galaxies is accreted post-quenching. Except for the first, all of them lie in the SDSS region. We applied our AI method to their optical images and found that all of them are classified as RFI galaxies. Moreover, all seven galaxies have an HI size apparently larger than that of the stellar component⁸. It hints that the newly accreted gas has large angular momentum.

Data availability The optical images are taken from <https://skyserver.sdss.org/dr17/VisualTools/list>. The stellar mass for SDSS galaxies is publicly available at <https://wwwmpa.mpa-garching.mpg.de/SDSS/DR7/>. The star-formation rate for SDSS galaxies is publicly available at <https://salims.pages.iu.edu/gswlc/>. The galaxy sizes and velocity dispersion data can be downloaded at <http://sdss.physics.nyu.edu/vagc/>. MaNGA data is available at https://data.sdss.org/sas/dr17/manga/spectro/pipe3d/v3_1_1/3.1.1/. The representative xGASS sample can be downloaded at <https://xgass.icrar.org/data.html>. The galaxy group catalog is publicly available at <https://gax.sjtu.edu.cn/data/Group.html>. The DECaLS shear catalog is publicly available

at <https://gax.sjtu.edu.cn/data/DESI.html>. The axis ratio data is publicly available at <https://nadc.china-vo.org/casjobs/>.

Code availability The custom codes used in this paper are available upon request.

1. Fabian, A. C. Observational Evidence of Active Galactic Nuclei Feedback. *ARAA* **50**, 455–489 (2012). [1204.4114](#).
2. Heckman, T. M. & Best, P. N. The Coevolution of Galaxies and Supermassive Black Holes: Insights from Surveys of the Contemporary Universe. *ARAA* **52**, 589–660 (2014). [1403.4620](#).
3. Eckert, D., Gaspari, M., Gastaldello, F., Le Brun, A. M. C. & O’Sullivan, E. Feedback from Active Galactic Nuclei in Galaxy Groups. *Universe* **7**, 142 (2021). [2106.13259](#).
4. McNamara, B. R. & Nulsen, P. E. J. Heating Hot Atmospheres with Active Galactic Nuclei. *ARAA* **45**, 117–175 (2007). [0709.2152](#).
5. Bîrzan, L., McNamara, B. R., Nulsen, P. E. J., Carilli, C. L. & Wise, M. W. Radiative Efficiency and Content of Extragalactic Radio Sources: Toward a Universal Scaling Relation between Jet Power and Radio Power. *ApJ* **686**, 859–880 (2008). [0806.1929](#).
6. Pinjarkar, S. *et al.* Spectral age distribution for radio-loud active galaxies in the XMM-LSS field. *MNRAS* **523**, 620–639 (2023). [2305.07561](#).
7. Su, K.-Y. *et al.* Which AGN jets quench star formation in massive galaxies? *MNRAS* **507**, 175–204 (2021). [2102.02206](#).
8. Serra, P. *et al.* The ATLAS^{3D} project - XIII. Mass and morphology of H I in early-type galaxies as a function of environment. *MNRAS* **422**, 1835–1862 (2012). [1111.4241](#).
9. Li, X. *et al.* On the Existence, Rareness, and Uniqueness of Quenched H I-rich Galaxies in the Local Universe. *ApJ* **963**, 86 (2024).
10. Croton, D. J. *et al.* The many lives of active galactic nuclei: cooling flows, black holes and the luminosities and colours of galaxies. *MNRAS* **365**, 11–28 (2006). [astro-ph/0508046](#).

11. Davé, R. *et al.* SIMBA: Cosmological simulations with black hole growth and feedback. *MNRAS* **486**, 2827–2849 (2019). [1901.10203](#).
12. Best, P. N. & Heckman, T. M. On the fundamental dichotomy in the local radio-AGN population: accretion, evolution and host galaxy properties. *MNRAS* **421**, 1569–1582 (2012). [1201.2397](#).
13. Best, P. N., von der Linden, A., Kauffmann, G., Heckman, T. M. & Kaiser, C. R. On the prevalence of radio-loud active galactic nuclei in brightest cluster galaxies: implications for AGN heating of cooling flows. *MNRAS* **379**, 894–908 (2007). [astro-ph/0611197](#).
14. Sabater, J. *et al.* The LoTSS view of radio AGN in the local Universe. The most massive galaxies are always switched on. *A&A* **622**, A17 (2019). [1811.05528](#).
15. Zhang, C. *et al.* Nearly all Massive Quiescent Disk Galaxies Have a Surprisingly Large Atomic Gas Reservoir. *ApJL* **884**, L52 (2019). [1910.02093](#).
16. Hardcastle, M. J. *et al.* Radio AGN selection in LoTSS DR2. *MNRAS* **539**, 1856–1878 (2025). [2504.09303](#).
17. Brinchmann, J. *et al.* The physical properties of star-forming galaxies in the low-redshift Universe. *MNRAS* **351**, 1151–1179 (2004). [astro-ph/0311060](#).
18. Renzini, A. & Peng, Y.-j. An Objective Definition for the Main Sequence of Star-forming Galaxies. *ApJL* **801**, L29 (2015). [1502.01027](#).
19. Quici, B., Turner, R. J., Seymour, N. & Hurley-Walker, N. AGN energetics and lifetimes from remnant radio galaxies. *MNRAS* **537**, 343–363 (2025). [2405.11777](#).
20. York, D. G. *et al.* The Sloan Digital Sky Survey: Technical Summary. *AJ* **120**, 1579–1587 (2000). [astro-ph/0006396](#).
21. Abazajian, K. N. *et al.* The Seventh Data Release of the Sloan Digital Sky Survey. *ApJS* **182**, 543–558 (2009). [0812.0649](#).
22. Yang, X. *et al.* Galaxy Groups in the SDSS DR4. I. The Catalog and Basic Properties. *ApJ* **671**, 153–170 (2007). [0707.4640](#).

23. Krizhevsky, A., Sutskever, I. & Hinton, G. E. Imagenet classification with deep convolutional neural networks. *Advances in neural information processing systems* **25** (2012).
24. Szegedy, C. *et al.* Going deeper with convolutions. In *Proceedings of the IEEE conference on computer vision and pattern recognition*, 1–9 (2015).
25. Zhong, Z., Zheng, L., Kang, G., Li, S. & Yang, Y. Random erasing data augmentation. In *Proceedings of the AAAI conference on artificial intelligence*, vol. 34, 13001–13008 (2020).
26. Wang, Y. *et al.* Symmetric cross entropy for robust learning with noisy labels. In *Proceedings of the IEEE/CVF international conference on computer vision*, 322–330 (2019).
27. Turner, R. J. & Shabala, S. S. Energetics and Lifetimes of Local Radio Active Galactic Nuclei. *ApJ* **806**, 59 (2015). [1504.05204](#).
28. Bundy, K. *et al.* Overview of the SDSS-IV MaNGA Survey: Mapping nearby Galaxies at Apache Point Observatory. *ApJ* **798**, 7 (2015). [1412.1482](#).
29. Barišić, I. *et al.* An Absence of Radio-loud Active Galactic Nuclei in Geometrically Flat Quiescent Galaxies: Implications for Maintenance-mode Feedback Models. *ApJL* **872**, L12 (2019). [1902.00515](#).
30. Hong, H. *et al.* Dynamical Hotness, Star Formation Quenching, and Growth of Supermassive Black Holes. *ApJ* **954**, 183 (2023). [2305.02910](#).
31. Mandelbaum, R., Li, C., Kauffmann, G. & White, S. D. M. Halo masses for optically selected and for radio-loud AGN from clustering and galaxy-galaxy lensing. *MNRAS* **393**, 377–392 (2009). [0806.4089](#).
32. Zhang, J. *et al.* Testing shear recovery with field distortion. *The Astrophysical Journal* **875**, 48 (2019). URL <https://doi.org/10.3847/1538-4357/ab1080>.
33. Shankar, F. *et al.* Constraining black hole-galaxy scaling relations and radiative efficiency from galaxy clustering. *Nature Astronomy* **4**, 282–291 (2020). [1910.10175](#).
34. Li, Q. *et al.* Black Hole–Halo Mass Relation from UNIONS Weak Lensing. *ApJL* **969**, L25 (2024). [2402.10740](#).

35. Yang, H. *et al.* Modeling the inner part of the jet in M87: Confronting jet morphology with theory. *Science Advances* **10**, eadn3544 (2024). [2403.15950](#).
36. Catinella, B. *et al.* xGASS: total cold gas scaling relations and molecular-to-atomic gas ratios of galaxies in the local Universe. *MNRAS* **476**, 875–895 (2018). [1802.02373](#).
37. Wang, T. *et al.* Black holes regulate cool gas accretion in massive galaxies. *Nature* **632**, 1009–1013 (2024). [2311.07653](#).
38. Catinella, B. *et al.* The GALEX Arecibo SDSS Survey - VIII. Final data release. The effect of group environment on the gas content of massive galaxies. *MNRAS* **436**, 34–70 (2013). [1308.1676](#).
39. Duc, P.-A. *et al.* The ATLAS^{3D} project - IX. The merger origin of a fast- and a slow-rotating early-type galaxy revealed with deep optical imaging: first results. *MNRAS* **417**, 863–881 (2011). [1105.5654](#).
40. Yang, M. *et al.* Dark matter measurements combining stellar and H I kinematics: 30 per cent 1σ outliers with low dark matter content at $5R_e$. *MNRAS* **528**, 5295–5308 (2024). [2401.17553](#).
41. Lu, S. *et al.* From large-scale environment to cgm angular momentum to star forming activities – ii. quenched galaxies. *MNRAS* **509**, 2707–2719 (2021). URL <https://doi.org/10.1093/mnras/stab3169>. [2109.06197](#).
42. Zhang, Z. *et al.* Massive star-forming galaxies have converted most of their halo gas into stars. *A&A* **663**, A85 (2022). [2112.04777](#).
43. Zhou, S. *et al.* Star Formation Histories of Massive Red Spiral Galaxies in the Local Universe. *ApJ* **916**, 38 (2021). [2011.13749](#).
44. Tanaka, T. S. *et al.* HINOTORI I: The nature of rejuvenation galaxies. *PASJ* **76**, 1–26 (2024). [2307.14235](#).
45. Pillepich, A. *et al.* Simulating galaxy formation with the IllustrisTNG model. *MNRAS* **473**, 4077–4106 (2018). [1703.02970](#).

46. Li, H., Chen, Y., Wang, H. & Mo, H. Physical Processes Behind the Co-Evolution of Halos, Galaxies and Supermassive Black Holes in the IllustrisTNG Simulation. *arXiv e-prints* arXiv:2409.06208 (2024). [2409.06208](#).
47. Weinberger, R. *et al.* Simulating galaxy formation with black hole driven thermal and kinetic feedback. *MNRAS* **465**, 3291–3308 (2017). [1607.03486](#).
48. Davies, L. J. M. *et al.* Galaxy And Mass Assembly: the 1.4 GHz SFR indicator, SFR- M_* relation and predictions for ASKAP-GAMA. *MNRAS* **466**, 2312–2324 (2017). [1701.06242](#).
49. Blanton, M. R. *et al.* New York University Value-Added Galaxy Catalog: A Galaxy Catalog Based on New Public Surveys. *AJ* **129**, 2562–2578 (2005). [astro-ph/0410166](#).
50. Yang, X., Mo, H. J., van den Bosch, F. C. & Jing, Y. P. A halo-based galaxy group finder: calibration and application to the 2dFGRS. *MNRAS* **356**, 1293–1307 (2005). [astro-ph/0405234](#).
51. Bezanson, R. *et al.* Redshift Evolution of the Galaxy Velocity Dispersion Function. *ApJL* **737**, L31 (2011). [1107.0972](#).
52. Shimasaku, K. *et al.* Statistical Properties of Bright Galaxies in the Sloan Digital Sky Survey Photometric System. *AJ* **122**, 1238–1250 (2001). [astro-ph/0105401](#).
53. Saglia, R. P. *et al.* The SINFONI Black Hole Survey: The Black Hole Fundamental Plane Revisited and the Paths of (Co)evolution of Supermassive Black Holes and Bulges. *ApJ* **818**, 47 (2016). [1601.00974](#).
54. Kauffmann, G. *et al.* The host galaxies of active galactic nuclei. *MNRAS* **346**, 1055–1077 (2003). [astro-ph/0304239](#).
55. Salim, S. *et al.* GALEX-SDSS-WISE Legacy Catalog (GSWLC): Star Formation Rates, Stellar Masses, and Dust Attenuations of 700,000 Low-redshift Galaxies. *ApJS* **227**, 2 (2016). [1610.00712](#).
56. Alam, S. *et al.* The Eleventh and Twelfth Data Releases of the Sloan Digital Sky Survey: Final Data from SDSS-III. *ApJS* **219**, 12 (2015). [1501.00963](#).

57. Lupton, R. *et al.* Preparing Red-Green-Blue Images from CCD Data. *PASP* **116**, 133–137 (2004). [astro-ph/0312483](#).
58. Condon, J. J. *et al.* The NRAO VLA Sky Survey. *AJ* **115**, 1693–1716 (1998).
59. Becker, R. H., White, R. L. & Helfand, D. J. The FIRST Survey: Faint Images of the Radio Sky at Twenty Centimeters. *ApJ* **450**, 559 (1995).
60. Condon, J. J., Cotton, W. D. & Broderick, J. J. Radio Sources and Star Formation in the Local Universe. *AJ* **124**, 675–689 (2002).
61. He, K., Zhang, X., Ren, S. & Sun, J. Deep residual learning for image recognition. In *Proceedings of the IEEE conference on computer vision and pattern recognition*, 770–778 (2016).
62. Hermans, A., Beyer, L. & Leibe, B. In defense of the triplet loss for person re-identification. *arXiv preprint arXiv:1703.07737* (2017).
63. Jin, G., Kauffmann, G., Best, P. N., Shenoy, S. & Małek, K. The host galaxies of radio AGN: New views from combining LoTSS and MaNGA observations. *A&A* **694**, A309 (2025). [2409.01279](#).
64. Hardcastle, M. J. *et al.* The LOFAR Two-Metre Sky Survey. VI. Optical identifications for the second data release. *A&A* **678**, A151 (2023). [2309.00102](#).
65. Wang, T. *et al.* Science with the 2.5-meter Wide Field Survey Telescope (WFST). *Science China Physics, Mechanics, and Astronomy* **66**, 109512 (2023). [2306.07590](#).
66. Abdurro’uf *et al.* The Seventeenth Data Release of the Sloan Digital Sky Surveys: Complete Release of MaNGA, MaStar, and APOGEE-2 Data. *ApJS* **259**, 35 (2022). [2112.02026](#).
67. Sánchez, S. F. *et al.* Pipe3D, a pipeline to analyze Integral Field Spectroscopy Data: II. Analysis sequence and CALIFA dataproducts. *Rev. Mexicana Astron. Astrofis.* **52**, 171–220 (2016). [1602.01830](#).
68. Blanton, M. R., Kazin, E., Muna, D., Weaver, B. A. & Price-Whelan, A. Improved Background Subtraction for the Sloan Digital Sky Survey Images. *AJ* **142**, 31 (2011). [1105.1960](#).

69. Dey, A. *et al.* Overview of the DESI Legacy Imaging Surveys. *AJ* **157**, 168 (2019). [1804.08657](#).
70. Zou, H., Gao, J., Zhou, X. & Kong, X. Photometric redshifts and stellar masses for galaxies from the DESI legacy imaging surveys. *The Astrophysical Journal Supplement Series* **242**, 8 (2019). URL <https://doi.org/10.3847/1538-4365/ab1847>.
71. Zhang, J., Luo, W. & Foucaud, S. Accurate shear measurement with faint sources. *JCAP* **2015**, 024 (2015). [1312.5514](#).
72. Wang, H., Zhang, J., Li, H. & Shen, Z. Avoiding the Geometric Boundary Effect in Shear Measurement. *ApJ* **911**, 10 (2021). [2012.11322](#).
73. Zhang, J. *et al.* Shear Measurement with Poorly Resolved Images. *AJ* **164**, 128 (2022). [2206.02434](#).
74. Zhang, J., Zhang, P. & Luo, W. Approaching the Cramér-Rao Bound in Weak Lensing with PDF Symmetrization. *ApJ* **834**, 8 (2017). [1606.09397](#).
75. Mandelbaum, R. *et al.* Strong bimodality in the host halo mass of central galaxies from galaxy-galaxy lensing. *MNRAS* **457**, 3200–3218 (2016). [1509.06762](#).
76. Luo, W. *et al.* Galaxy-Galaxy Weak-lensing Measurements from SDSS. II. Host Halo Properties of Galaxy Groups. *ApJ* **862**, 4 (2018). [1712.09030](#).
77. Navarro, J. F., Frenk, C. S. & White, S. D. M. A Universal Density Profile from Hierarchical Clustering. *ApJ* **490**, 493–508 (1997). [astro-ph/9611107](#).
78. Tinker, J. L. *et al.* The Large-scale Bias of Dark Matter Halos: Numerical Calibration and Model Tests. *ApJ* **724**, 878–886 (2010). [1001.3162](#).
79. Foreman-Mackey, D., Hogg, D. W., Lang, D. & Goodman, J. emcee: The MCMC Hammer. *PASP* **125**, 306 (2013). [1202.3665](#).
80. Haynes, M. P. *et al.* The arecibo legacy fast alfa survey: The alfa extragalactic h i source catalog. *The Astrophysical Journal* **861**, 49 (2018).

81. Sánchez, S. F. *et al.* SDSS-IV MaNGA: pyPipe3D Analysis Release for 10,000 Galaxies. *ApJS* **262**, 36 (2022). [2206.07062](#).
82. Cappellari, M. Effect of Environment on Galaxies' Mass-Size Distribution: Unveiling the Transition from outside-in to inside-out Evolution. *ApJL* **778**, L2 (2013). [1309.1136](#).
83. Kokusho, T. *et al.* A star formation study of the ATLAS^{3D} early-type galaxies with the AKARI all-sky survey. *A&A* **605**, A74 (2017). [1705.10521](#).
84. Leroy, A. K. *et al.* A $z = 0$ Multiwavelength Galaxy Synthesis. I. A WISE and GALEX Atlas of Local Galaxies. *ApJS* **244**, 24 (2019). [1910.13470](#).

Acknowledgements We thank Meng Yang and DanDan Xu for useful discussion. HYW is supported by the National Natural Science Foundation of China (NSFC, Nos. 12192224) and CAS Project for Young Scientists in Basic Research, Grant No. YSBR-062. YL and WLOY are supported by the JC STEM Lab of AI for Science and Engineering, funded by The Hong Kong Jockey Club Charities Trust, the Research Grants Council of Hong Kong (Project No. CUHK14213224). JW thanks support of research grants from Ministry of Science and Technology of the People's Republic of China (NO. 2022YFA1602902), NSFC (NO. 12233001), and the China Manned Space Project (No. CMS-CSST-2025-A08). ECW thanks support of the National Science Foundation of China (Nos. 12473008) and the Start-up Fund of the University of Science and Technology of China (No. KY2030000200). HXZ acknowledges support from the National Key Research and Development Program of China (grant No. 2023YFA1608100), and from the NSFC (grant Nos. 12122303, 11973039). YYC is funded by the China Postdoctoral Science Foundation (grant No. 2022TQ0329) The authors gratefully acknowledge the support of Cyrus Chun Ying Tang Foundations. The work is also supported by the Supercomputer Center of University of Science and Technology of China.

Competing Interests The authors declare that they have no competing financial interests.

Author Contributions The listed authors made substantial contributions to this manuscript; all co-authors read and commented on the document. HYW is responsible for the original idea, led the analysis and wrote the draft. HLL compiled and analyzed the observational data, developed the methods for purity and made the figures. YL developed and implemented the AI method and wrote the section for the AI method. HH compiled and analyzed the observational data. HLL, YL and HH contribute equally to this work, and YL

and HH are co-first authors. HJM contributed to the writing and interpretation of results. JW contributed to the analysis of HI data and interpretation of the results. WLOY contributed to the development of the AI method. ZWZ and QXL contributed to the analysis of weak lensing. ECW, HXZ, YYC, HL and MKZ contributed to the interpretation of the results.

Correspondence Correspondence and requests for materials should be addressed to HYW (email: whywang@ustc.edu.cn).